UNIVERSITY OF CALIFORNIA
RIVERSIDE

Exploring Magnetism in Metal-Rich Borides: Synthesis, Characterization, and Magnetic Properties

A Dissertation submitted in partial satisfaction
of the requirements for the degree of

Doctor of Philosophy

in

Chemistry

by

Diana Luong

September 2023

Dissertation Committee:
Dr. Boniface Fokwa, Chairperson
Dr. Tim Su
Dr. Hill Harmen

The Dissertation of Diana Luong is approved:

_____

_____

_____

Committee Chairperson

University of California, Riverside

Acknowledgements

I acknowledge the San Diego Supercomputer Center (SDSC) for providing computing resources and the financial support by NSF (DMR-1654780) for making this work possible. I acknowledge the help of Dr. Rainer Pöttgen and Dr. Elena Haddon with assistance in running the magnetic measurements. I would like to thank all co-authors for their contributions in the manuscripts listed below:

Amir A. Rezaie, Eunsoo Lee, Diana Luong, Johan A. Yapo, Boniface P. T. Fokwa. "Abundant Active Sites on the Basal Plane and Edges of Layered van der Waals Fe_3GeTe_2 for Highly Efficient Hydrogen Evolution", ACS Materials Letters 2021

Eunsoo Lee, Amir A. Rezaie, Diana Luong, Johan A. Yapo, Boniface P. T. Fokwa. "$Fe_5Ge_2Te_2$: Iron-rich Layered Chalcogenide for Highly Efficient Hydrogen Evolution", Z. Anorg. Allg. Chem. 2022

Diana Luong, Sam Kilic, Elena Haddon, Boniface P. T. Fokwa. Role of Hafnium and Magnetic Characteristics in Quinary System $Hf_2Fe_{1-\delta}Ir_{5-x+\delta}Ru_xB_2$. Manuscript in preparation

Diana Luong, Michael Küpers, Rainer Pöttgen, Boniface P. T. Fokwa. Synthesis and Magnetic Properties of the Transition Metal-Rich Boride$Ti_2FeOs_3B_3$. Manuscript in preparation

I extend my gratitude to all co-authors of the additional manuscripts published while at UC Riverside. The following list comprises of manuscripts that are not explicitly part of the dissertation:

Ledoux S. Pouamo, Carole F.N. Nguemdzi, Mohammad Azam, Diana Luong, Kate A. Gibson, Wangxiang Li, Elena B. Haddon, Boniface P.T. Fokwa, Justin Nenwa. "Two high-spin cobalt(III) complex anions with pyridinium-based cations: synthesis, structural elucidation and magnetic properties", J. Mol. Str. 2022

Anh N. Hong, Diana Luong, Mohammed Alghamdi, Wei-Cheng Liao, Weiyi Zhang, Emily Kusumoputro, Yichong Chen, P. Alex Greaney, Yongtao Cui, Jing Shi, Xianhui Bu, Boniface P.T. Fokwa, Pingyun Feng. “Metal-mediated Directional-capping of Rod-packing Metal-organic Frameworks”, Chem. Eur. J. 2022

Youming Xu, Zahra Barani, Penghao Xiao, Sriharsha Sudhindra, Yitian Wang, Amir Rezaie, Veronica Carta, Krassimir Bozhilov, Diana Luong, Boniface Fokwa, Fariborz Kargar, Alexander Balandin, Xi Chen. “Crystal Structure and Thermoelectric Properties of Layered van der Waals Semimetal ZrTiSe4”, Chem. Mat. 2022

I am profoundly grateful to all individuals who have supported me throughout this journey of completing my dissertation. I am thankful to Robert Corn, Shane Ardo, and Charles Deneke for their help and guidance as I pursued my aspirations for graduate school. Their contributions are what got me to where I am now. I extend my deepest gratitude to my supervisor, Boniface Fokwa, for five years of mentorship, patience, and expertise that led me to embrace my love for boron. I am also thankful to my dissertation committee, Tim Su and Hill Harmen, for their time and input.

I want to express my thanks to my friends and colleagues for being a source of motivation; this work is a testament to the collective effort of all those who have supported me. Special thanks to Eunsoo Lee, Ardalan Rezaie, Sang Bum Kim, Johan Yapo, Kate Gibson, Ashwin Bhupathy, Paul Isaac, Sam Kilic, and everyone else I’ve worked with. It’s been a journey in the Fokwa lab. Thank you, Shivansh Kaushik, for listening to my science talks and starting my gym arc. I would like to thank coaches Sreekar Vattipalli, Brian Vu, Tao Arellano, and Alex MacDonald for the mind to mooscle connection. Education is important, but big biceps is importanter. Thank you, Jim, for the

resistance band and all the cake. Thank you, husband Pengxiong Zhu, as he requires a green card. Thank you my king, Sam Xiang, as he's a great mechanic and chauffeur. Thank you, Andrew Crago, John Speigel, and Michelangelo Landgrave for being there at the start of the tabletop journey. To all others who joined along the way, it brings me joy to have crossed paths with each of you. Thank you.

Diana Luong

September 2023

ABSTRACT OF THE DISSERTATION

Exploring Magnetism in Metal-Rich Borides: Synthesis, Characterization, and Magnetic Properties

by

Diana Luong

Doctor of Philosophy, Graduate Program in Chemistry
University of California, Riverside, September 2023
Dr. Boniface Fokwa, Chairperson

Rare-earth elements possess unique magnetic, optical, and electronic properties, making them essential components in modern technologies, including but not limited to electronics, renewable energy systems, and telecommunications. However, the supply of rare-earth elements is limited, and their extraction and processing can have significant environmental impact. Addressing this challenge is the exploration of new magnetic compounds which aims to reduce dependence on rare-earth elements. The research presented in this study focuses on the synthesis and characterization of new metal-rich borides, exploring their potential as possible magnets. Because of the versatility of metal borides, these compounds have applications in fields such as permanent magnets, superconductors, and conductive ceramics.

The $Ti_3Co_5B_2$ structure-type is one of many metal-rich borides that represents an effort to search for magnetic materials that could replace the rare-earth elements. Consisting of a layered arrangement of titanium, cobalt, and boron atoms, this compound can introduce magnetically active elements. New quinary members based on this structure, $Hf_2Fe_{1-\delta}Ir_{5-x+\delta}Ru_xB_2$ (x = 1-4, VE = 63-66), were synthesized and investigated for the possibility of magnetic tuning using non-magnetic elements. All compounds exhibited intrinsic soft to semi-hard magnetic behaviors with notable hysteresis even at room temperature. Another metal-rich boride, $Ti_2FeOs_3B_3$, was synthesized to understand its structural and magnetic characteristics. This compound features isolated boron, B_4 zigzag fragments, iron dumbbell chains, and osmium. Coupled with theoretical calculations, this work contributes to the understanding of complex magnetic interactions. Finally, by leveraging computational techniques, the exploration of new compounds such as $Hf_2FeOs_5B_2$ and $Hf_2MnOs_5B_2$ within the $Ti_3Co_5B_2$ structure-type has been investigated. By predicting and understanding these new materials, their potential suitability can be discerned.

Table of Contents

List of Tables

List of Figures

Chapter 1:

Introduction

1.1 Introduction to Magnetism

Magnets are crucial components in numerous modern technologies, including but not limited to cell phones, transformers, and medical devices.[1–3] In typical permanent magnets, rare-earth elements such as neodymium and dysprosium are relied on due to their high maximum energy product, and their presence is vital to enhance magnet performance. However, the availability and extraction difficulties of these elements make them insecure sources. Increasing demand for high-performance permanent magnets (PMs) is resulting in economic pressure on their supply and environmental impact. Consequently, efforts are underway to search for alternative permanent magnetic materials that are free from rare-earths elements and expensive metals.[2] Thus, rare-earth (RE) free materials involving Fe, Ni, and Mn are strategic candidates for developing improved magnets. While these materials may not have the same strength as RE magnets, they have a lower cost, lower toxicity, and greater abundance. There is a strong motivation to drive the development of next-generation RE-free PMs that are lightweight, have a high energy product, are mechanically machinable, and corrosion-resistant.[1,4–6]

1.2 Magnetic Moment

It is essential to identify parameters that characterize the response of the magnetic material to an applied magnetic field. Magnetic forces originate in regions called poles, which are located near the ends of, say, a bar magnet. Poles always occur in pairs, and it is impossible to separate them. A magnetic field is created by a magnetic pole, which pervades the region around the pole. This field causes a force on the second pole nearby which is directly proportional to the product of the pole strength *p* and field intensity $\vec{H}$. Let us consider a bar magnet with pole strength p and separated by a distance l, which is placed at an angle θ to a uniform field $\vec{B} = \mu_0 \vec{H}$ (Figure 1).

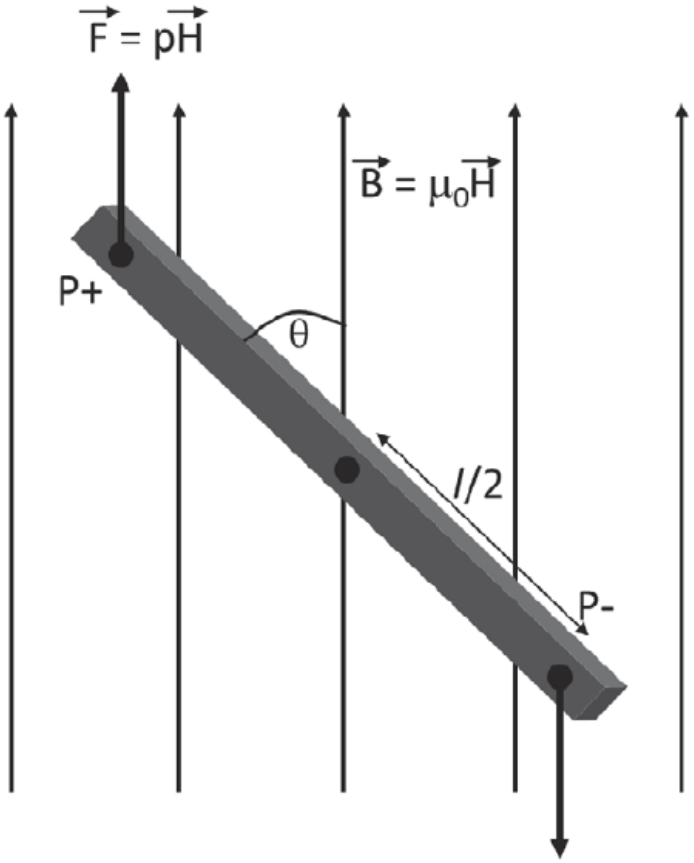

Figure 1.1: Schematic presentation of a bar magnet in a uniform magnetic field (reproduced from [4]).

The moment of this torque is

$$\mu = pHlsin\theta$$

The magnetic moment of a magnet is defined as the moment of the torque experienced by the magnet when it is at right angles to a uniform field of 1 Oe. The magnetic moment μ is a vector, and in vector notation, the energy equation is written as

$$E_p = -\vec{\mu}.\vec{H}$$

If the energy E_p is expressed in ergs, then the unit of magnetic moment μ is erg/oersted. This quantity is the electromagnetic unit of magnetic moment and is generally termed simply as *emu*.

The total magnetic moment is the sum of the magnetic moments of the individual magnets. The magnetic moment is thus doubled by doubling the volume. However, the magnetic moment per unit volume is not changed, and therefore this is a quantity that describes the degree to which the magnets are magnetized. This is termed as the intensity of magnetization, or simply magnetization, and is expressed as $\vec{M}$. The unit of $\vec{M}$ is erg/oersted cm^3, but more often written simply as emu/cm^3. In small volumes like the unit cell of magnetic solids, the magnetic moment is often expressed in a unit called Bohr magnetons. Bohr magneton is a suitable unit for the estimation of the size of atomic magnetic moment and it takes the value of 9.274×10^{-24} Am^2.[4,7]

1.3 Non-ferromagnets

Magnetic solids can be classified into two main groups based on their magnetic properties: non ferromagnets and ferromagnets. Nonferromagnetic materials consist of diamagnets and Pauli paramagnets, which do not exhibit spontaneous magnetization or have a high magnetic susceptibility. Both diamagnetic and paramagnetic materials are generally considered to be non-magnetic as their magnetic properties are relatively weak.

Diamagnetic materials have filled atomic shells and no unpaired electrons. Thus, the atoms have no intrinsic magnetic moment in the absence of an external magnetic

field. An applied magnetic field induces a magnetic moment that opposes this applied field. With increasing temperature, there will also be a contribution to diamagnetic susceptibility from states above the ground state, but it's relatively small and thus largely considered temperature independent.

Paramagnetic materials have unpaired electrons and thus an intrinsic magnetic moment. Applying an external magnetic field will align such moments parallel to the direction of the field, and it corresponds to a positive magnetic susceptibility. The degree of alignment increases with increase in field strength, while an increase in temperature will randomize these alignments. Therefore, the alignment of magnetic moments will depend on the ratio B/T, where B is the magnetic field strength and T is temperature. In the absence of a magnetic field, the magnetic moments of the atoms will point to random directions, giving a net magnetization of zero or negligible.[4]

1.4 Ferromagnet

Ferromagnets are compounds with spontaneous magnetic order even in the absence of an external magnetic field and all the magnetic moments tend to point towards a single direction. The latter phenomenon is not necessarily valid strictly in all ferromagnets throughout the sample because they consist of several small regions known as domains. There exist boundaries called domain walls separating the domains, as shown in Figure 2. Within individual domains, the magnetic moments are aligned in the same direction, but the magnetization of each domain may point towards a different direction

than its neighbor. Ferromagnetism is frequently encountered in metals such as Fe, Co, Ni as well as alloys such as PtCo and $SmCo_5$.

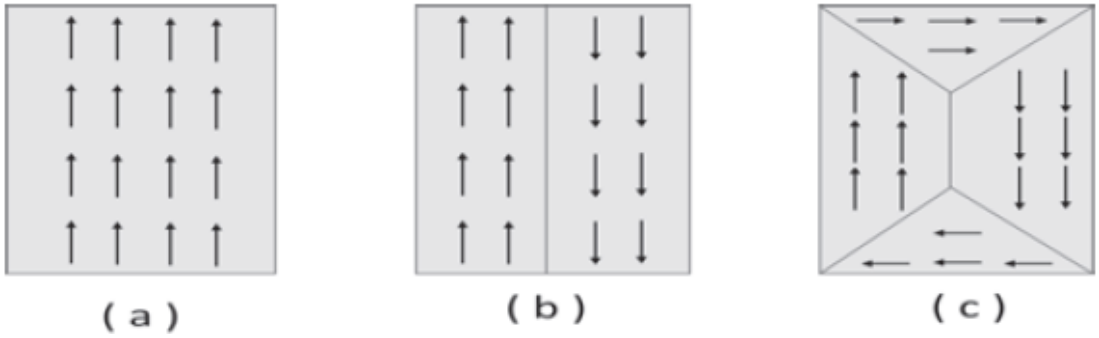

Figure 1.2: Schematic representation of domain structures: (a) single-domain structure, (b) two-domain structure, and (c) four-domain structure (reproduced from [4]).

As temperature increases for ferromagnets, thermal fluctuations will progressively disturb the magnetic moments. At a critical temperature, the ferromagnetic order will be destroyed completely, which is known as the Weiss model of ferromagnetism. Above this critical temperature T_C, or Curie temperature, ferromagnetic materials behave like a paramagnet. Magnetization is non-zero in the temperature regime $T < T_C$ and becomes zero for $T \geq T_C$. Magnetic susceptibility of a ferromagnetic sample follows the Curie–Weiss law:

$$\chi \text{int} = \frac{\text{C}}{T - Tc}$$

where C is the Curie constant and T_C is the Curie temperature.

When applying a small magnetic field, the domains are rearranged and reoriented in the direction of the applied field at the expense of the domains of the other orientation by smooth movement of the domain walls. This growth of the favorably oriented domain is shown on the right-hand side of Figure 3. Withdrawing the magnetic field causes the

domains to go back to their previous configuration with net bulk magnetization zero for the whole sample. If the applied field is not very weak, the growth of favorably oriented domains may take place through irreversible processes. The domain walls can pass through crystalline defects and imperfections if the external field is sufficiently large. On further increase of the applied magnetic field, the magnetization direction within the domains tends to rotate to the direction of the applied field. Despite the expenditure of magnetic anisotropy energy, the rotation of the entire domain towards the applied field direction may become energetically favorable, reaching a state of saturation magnetization. Once this occurs, it may be difficult for a ferromagnetic material to get back to the multi-domain configuration on the removal of the external magnetic field.

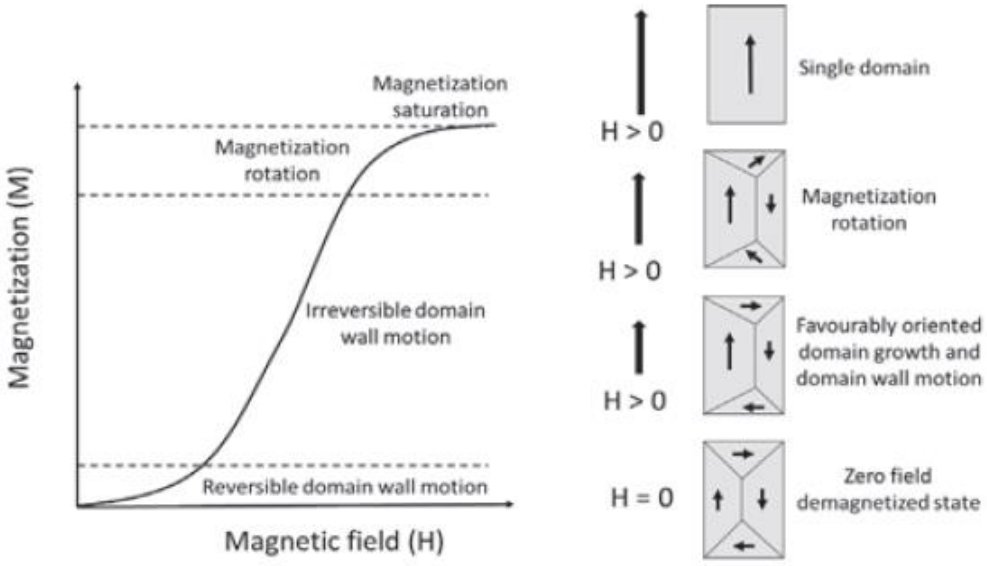

Figure 1.3: Magnetization process of a ferromagnetic sample with the variation of magnetization with applied magnetic field, and the associated changes in the domain configuration (reproduced from [4]).

Some residual domain structures are often left within the material during the magnetization cycle, and such structures act as nucleation centers for the growth of reverse domains through the motion of the walls. When the external field is removed, crystalline defects will impede the motion of the domains to return to their original unmagnetized configuration in zero fields, giving rise to magnetic history dependence or hysteresis in magnetization as seen in Figure 4. A residual magnetization or remanent magnetization, M_{Rem} is left with reducing the applied magnetic field back to zero. To restore the zero-magnetization state, a strong negative magnetic field called "coercive field (H_{Coer})" is needed.[4]

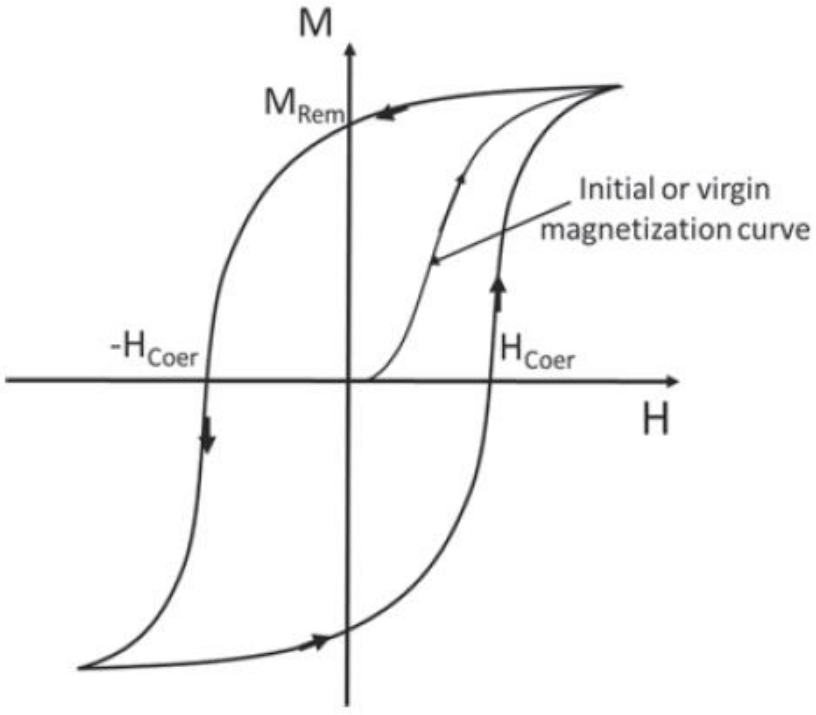

Figure 1.4: Schematic presentation of isothermal field variation of magnetization in real ferromagnetic materials with crystalline defects. Magnetization shows distinct field hysteresis characterized by remanent magnetization M_{Rem} and coercive field H_{Coer} (reproduced from [4]).

1.5 Antiferromagnet

An antiferromagnet is a type of magnetic material in which the magnetic moments of neighboring atoms or ions align antiparallel to each other in an external field. It's caused by negative interatomic exchange constants, but the different sublattices are chemically and crystallographically equivalent. For example, CoO crystallizes in the rock-salt structure, but the Co forms two sublattices of equal and opposite magnetization. Unlike a ferromagnet, this results in a net magnetic moment of zero and does not lead to an energetic advantage for the moments to line up. The difference of the level of magnetization creates a "staggered magnetization", which is non-zero in the temperature region below the Neel temperature (T_N) and is akin to the spontaneous magnetization of ferromagnets.

In the sublattice magnetizations, $|M_+| = |M_-| = M_S$, M+ and M- corresponds to the antiparallel spin alignment, and Ms is the saturation magnetization. In an applied magnetic field, the field will be antiparallel to the magnetization direction of the other sublattice, causing a small term to be added or subtracted from the local field of each sublattice. This has overall no effect since both sublattices are already saturated and net induced magnetization is zero so that parallel susceptibility $\chi_{\parallel} = 0$. In the event of increasing temperature (and $T < T_N$), thermal fluctuations will decrease the molecular field in each sublattice. The applied magnetic field will then enhance the magnetization of the sublattice to which it is parallel while reducing the magnetization of the other,

creating a non-zero parallel susceptibility $\chi_{\parallel}$. This value will rise with increasing temperature, reaching a maximum value at $T = T_N$. [4]

1.6 Ferrimagnet

A ferrimagnet is if two sublattices are not equivalent due to some crystallographic reasons, and thus the magnetizations will not be equal. The material will display a net magnetization because the sublattices do not cancel out, such as Fe and Dy sublattices in $Dy_2Fe_{14}B$. The spontaneous magnetization of each sublattice will have different temperature dependences since the molecular field on each sublattice is different, leading to a net magnetization. Ferrimagnets have complicated temperature dependencies and magnetic susceptibilities which in general do not follow the Curie-Weiss law. Figure 5 displays the various magnetic orders. [4,5]

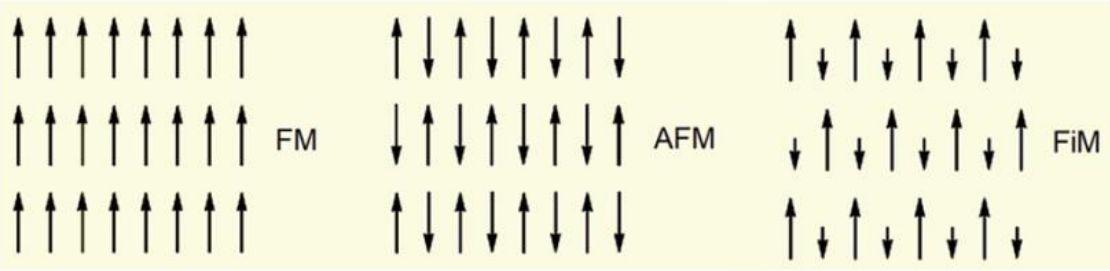

Figure 1.5: Spin structures (schematic): ferromagnets (FM), antiferromagnet (AFM), ferrimagnet (FiM) (reproduced from [5]).

1.7 Magnetic Properties

Understanding the metallurgical processing, phase stability, and microstructural changes is critical for developing and improving PMs. To design a high-performance permanent magnet, it's crucial to optimize key magnetic properties: saturation magnetic polarization (J_s), magnetic anisotropy energy (MAE), and Curie temperature (T_C). These macroscopic properties are derived from microscopic magnetic properties such as local magnetic moment, spin-orbit anisotropy energies, and magnetic exchange coupling.

A) Saturation magnetization is the maximum attainable magnetization of a ferromagnetic, which is achieved when all magnetic moments inside the material are aligned in parallel orientation. Any further increase in an external magnetic field will not result in an increase in magnetization. If there are *n* number of magnetic moments per unit volume, then the maximum magnetization that can be obtained by alignments of all the magnetic moments, i.e. saturation magnetic moment M_S, is represented as $Ms = n|\tilde{}\mu|$. The magnetic properties of a ferromagnetic crystal are anisotropic. Depending on the orientation of the magnetic field with respect to the symmetry axes of the crystal, the magnetization curve *M(H)* reaches saturation at low or high field values. The easy direction is which saturation is reached in a low field and the hard direction is when saturation requires a high field.

B) Magnetic anisotropy refers to the phenomenon where the energy of a magnetic object is determined by the orientation of its magnetization in

relation to its crystal axes or shape. Most magnetic materials are anisotropic, which can come from preferred crystal axes (magnetocrystalline anisotropy) or an axis that arises from some short-range ordering of atoms like Ni-Ni and Fe-Fe atomic pairs. Magnetocrysalline anisotropy is the primary contributor to anisotropy energy in most materials, which involves spin orbit coupling. It comprises of two steps: first, the magnetic moment-carrying electrons interact with the lattice through electrostatic crystal field and exchange interactions. Second, the spin-orbit coupling ensures that the spin magnetization aligns with the lattice. Other factors such as shape anisotropy and magnetoelastic anisotropy may also contribute to the overall anisotropy energy, but their effects are usually smaller than that of magnetocrystalline anisotropy.

C) The Curie-Weiss paramagnetic susceptibility can describe the behavior of many magnetic systems in external magnetic fields. When the temperature drops below the characteristic temperature for a crystal, which is the Curie temperature for ferromagnets and the Neel temperature for antiferro- and ferrimagnets, spontaneous ordering of magnetic moments occurs. For temperatures $T \leq T_C$, the experimentally measured susceptibility acquires a constant value

$$\chi exp = \frac{1}{N}$$

where N is the demagnetization factor. In a ferromagnetic sample, with an increase in aspect ratio, such as a cylindrical or rectangular shape, there is a decrease in the demagnetization factor N. One can observe a progressive

increase in the value of the measured susceptibility at T = T_C. Below T_C the temperature dependence of susceptibility is complex and influenced by other intrinsic properties, namely magnetic anisotropies. In high temperature cases, where one approaches the classical regime, the Curie–Weiss law is established in any case. A material is identified as a paramagnet if the Weiss temperature $\theta = 0$. On the other hand, if the material is

a ferromagnet (antiferromagnet), its Weiss temperature becomes $\theta = T_C$ ($\theta = -T_N$). Figure 6 (a) shows the expected temperature dependence of the susceptibility for paramagnet, ferromagnet, and antiferromagnet. Usually, it is the reciprocal susceptibility ($1/\chi$) that is plotted as a function of temperature, and the intercept of

the straight line on the temperature axis yields the value of the Weiss temperature.

(Figure 6 (b)).[4]

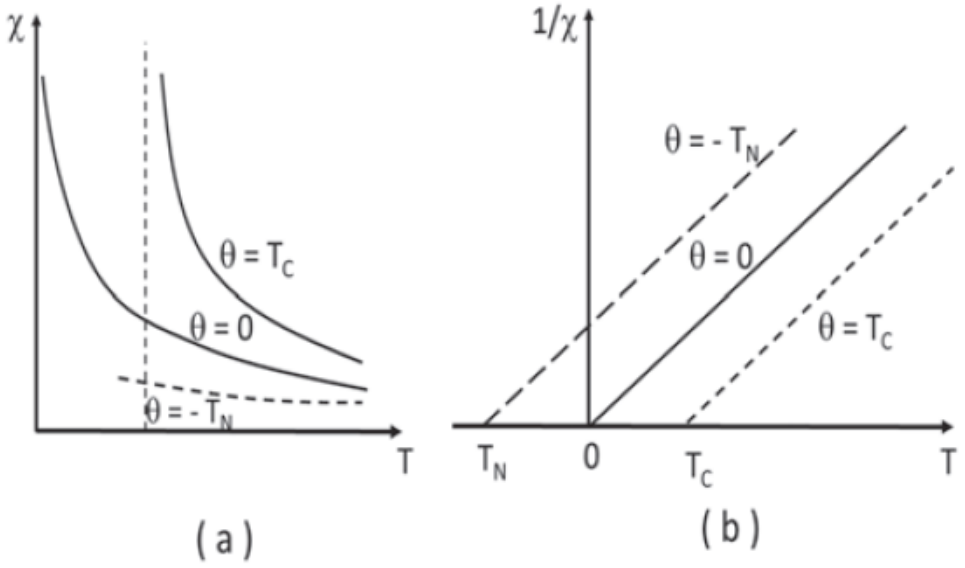

Figure 1.6: The Curie–Weiss law of magnetic susceptibility shown for three cases: paramagnet (θ= 0), ferromagnet ($\theta = T_C$) and antiferromagnet ($\theta = -T_N$). (b) Reciprocal susceptibility ($1/\chi$) versus temperature straight line plots with the intercept on the temperature axis yielding the Wiess temperature θ (reproduced from [4]).

1.8 Introduction to Metal-rich Boride $Ti_3Co_5B_2$

The surge in demand for high-performing permanent magnetic materials driven by emerging technologies such as electric vehicles, wind turbines, and magnetic refrigeration has spurred research efforts in the solid-state and materials communities to design and develop new materials. However, magnetism remains a complex phenomenon that is not yet fully understood. The reasons why some materials exhibit magnetic ordering while others do not continue to elude researchers. Despite the discovery of the strongest permanent magnet $Nd_2Fe_{14}B$ almost three decades ago, we still heavily rely on rare-earth elements such as Nd and Dy to produce the best-performing permanent

magnets, both of which have been designated as critical by the U.S. Department of Energy.[2,8–12] To address this issue, there is a growing movement towards developing more sustainable, rare-earth-free alternatives.

Metal borides (MxBy) encompass over 150 different structure types and thousands of compounds, which can be divided into boron-rich (B:M ≥ 4:1) and metal-rich (B:M < 4:1) categories. The crystal structure and arrangement of boron atoms play a vital role in determining the exceptional properties exhibited. Metal borides display various bonding patterns, including covalent B-B bonds, ionic M-B bonds, and even metallic M-M/M-B bonds. In metal-rich borides, an isolated boron atom is surrounded by a metal atom, while an increase in boron content leads to the formation of strong covalent B-B bonds and the emergence of one-dimensional boron chains, zigzags, two-dimensional sheets, and eventually three-dimensional boron networks.[13] These variations give rise to a diverse range of physiochemical properties such as high melting points, exceptional hardness, extraordinary magnetic properties, and remarkable chemical inertness.[14–18] Rare-earth-based borides containing magnetically active elements display strong permanent magnetic properties, while those with itinerant magnetism may have potential applications in magnetic refrigeration and spintronics. Due to their low cost and diverse range of structure types, metal borides are attractive for further exploration and are excellent candidates for use in electronics, catalysis, ion transport, and sensing.[12,19–21]

The $Ti_3Co_5B_2$ crystal structure is one of the most common structure types in metal-rich borides. It is a very hard material with excellent wear resistance, exhibiting

paramagnetic behavior. Crystallizing in the tetragonal space group P4/mbm, the structure has stacked alternating layers of Ti_3B_2 and Co_5. Within the unit cell, there are 20 atoms that occupy four distinct sites labeled 8j, 2c, 2a, and 4g. Displayed in Figure 7, the Ti atoms are found in the 4g and 2a sites, the Co atoms occupy the 2c and 8j sites, and the B atoms occupy the 2g sites.[22–25] The unit cell is compatible with several ordered compounds and many chemically disordered alloys.

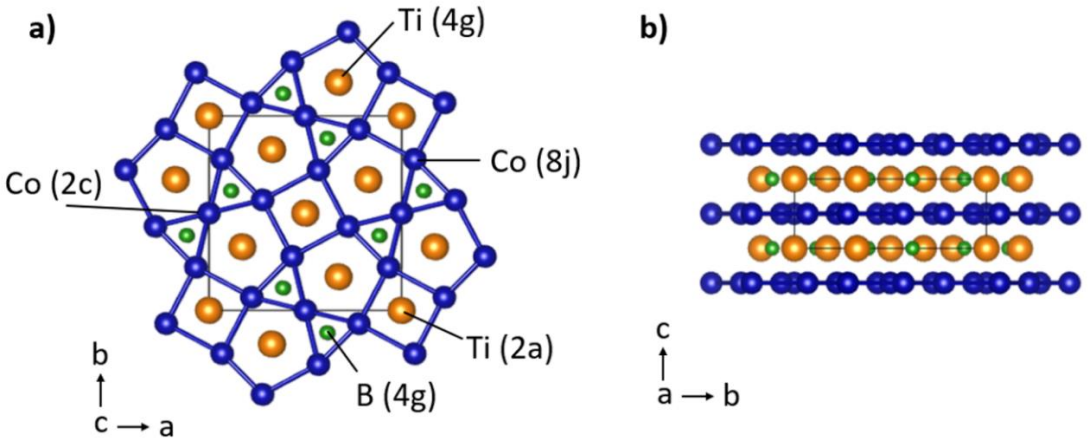

Figure 1.7: Crystal structures (unit cells) of $Ti_3Co_5B_2$: a) top-down view along (001) and b) side view along (100) direction.

The general formula, $A_3T_5B_2$, consists of T atoms occupied by a valence electron-rich transition metal like Co, Rh, or Ir. These 2c and 8j sites form pentagonal, tetragonal, and trigonal prisms that can be inhabited by other atoms. The A atoms are coordinated in the pentagonal (4g site) and tetragonal (2a site) configurations, while B atoms (4g site) are trigonally coordinated. The quaternary variant $A_2MT_5B_2$ introduces a magnetically active element M (e.g., Cr, Mn, Fe), which leads to a tetragonal-coordinated M position because atoms occupying the M position are usually smaller than those in the A

position.[24,26] This occupation with a magnetic element give rise to compounds with unique properties such as ferromagnetism in $Sc_2MnIr_5B_2$, anti-ferromagnetism in $Sc_2FeIr_5B_2$, or meta-magnetism in $Sc_2MnRh_5B_2$.[27] Over 60 compounds are known to adopt this crystal structure type, including the quaternary variant with the general formula $A_2MT_5B_2$ and quinary variant with the general formula $A_2M(TT')_5B_2$.[24]

This dissertation aims to develop novel magnetic materials based on the $Ti_3Co_5B_2$ structure type that do not contain rare-earth elements. Recently, a new quaternary boride, $Hf_2FeIr_5B_2$ (67 VE), was synthesized in the research group, which maximized the number of 5d elements and valence electron count. This phase displayed hysteresis above room temperature, making it a potential permanent magnetic material for future applications.[28] Chapter 3 focuses on the new quinary members of this Hf-series, $Hf_2FeIr_{5-x}Ru_xB_2$ (x = 0-5, VE = 62-67), detailing the magnetic characteristics as a function of valence electron count and the role of hafnium in this complex structure. Chapter 4 delves into the synthesis, characterization, and magnetic properties of $Ti_2FeOs_3B_2$. Finally, Chapter 5 examines the magnetic potential of a new possible compound $Hf_2MOs_5B_2$ (M = Mn, Fe).

References:

[1] Silveyra JM, Ferrara E, Huber DL, Monson TC. Soft magnetic materials for a sustainable and electrified world. Science 2018;362:eaao0195. https://doi.org/10.1126/science.aao0195.

[2] Gutfleisch O, Willard MA, Brück E, Chen CH, Sankar SG, Liu JP. Magnetic Materials and Devices for the 21st Century: Stronger, Lighter, and More Energy Efficient. Adv Mater 2011;23:821–42. https://doi.org/10.1002/adma.201002180.

[3] Giustino F, Lee JH, Trier F, Bibes M, Winter SM, Valentí R, et al. The 2021 quantum materials roadmap. J Phys Mater 2021;3:042006. https://doi.org/10.1088/2515-7639/abb74e.

[4] Roy SB. Experimental Techniques in Magnetism and Magnetic Materials n.d.

[5] Coey JMD, Parkin SSP, editors. Handbook of Magnetism and Magnetic Materials. Cham: Springer International Publishing; 2021. https://doi.org/10.1007/978-3-030-63210-6.

[6] Mohn P. Magnetism in the solid state: an introduction. Corrected 2nd printing. Berlin ; New York: Springer; 2006.

[7] Cullity BD, Graham CD. Introduction to magnetic materials. 2nd ed. Hoboken, N.J: IEEE/Wiley; 2009.

[8] Bhunia A, Gamer MT, Ungur L, Chibotaru LF, Powell AK, Lan Y, et al. From a Dy(III) Single Molecule Magnet (SMM) to a Ferromagnetic [Mn(II)Dy(III)Mn(II)] Trinuclear Complex. Inorg Chem 2012;51:9589–97. https://doi.org/10.1021/ic300065x.

[9] Herbst JF, Croat JJ, Yelon WB. Structural and magnetic properties of $Nd_2Fe_{14}B$ (invited). J Appl Phys 1985;57:4086–90. https://doi.org/10.1063/1.334680.

[10] Ma Y-J, Hu J-X, Han S-D, Pan J, Li J-H, Wang G-M. Manipulating On/Off Single-Molecule Magnet Behavior in a Dy(III)-Based Photochromic Complex. J Am Chem Soc 2020;142:2682–9. https://doi.org/10.1021/jacs.9b13461.

[11] PII: 0038-1098(84)90315-6 | Elsevier Enhanced Reader n.d. https://doi.org/10.1016/0038-1098(84)90315-6.

[12] Exploring rare earths supply constraints for the emerging clean energy technologies and the role of recycling | Elsevier Enhanced Reader n.d. https://doi.org/10.1016/j.jclepro.2014.04.035.

[13] Dronskowski R, Kikkawa S, Stein A. Handbook of Solid State Chemistry, 6 Volume Set. John Wiley & Sons; 2017.

[14] Hofmann K, Kalyon N, Kapfenberger C, Lamontagne L, Zarrini S, Berger R, et al. Metastable Ni_7B_3 : A New Paramagnetic Boride from Solution Chemistry, Its

Crystal Structure and Magnetic Properties. Inorg Chem 2015;54:10873–7. https://doi.org/10.1021/acs.inorgchem.5b01929.

[15] Zheng Q, Gumeniuk R, Borrmann H, Schnelle W, Tsirlin AA, Rosner H, et al. Ternary borides Nb $_7$ Fe $_3$ B $_8$ and Ta $_7$ Fe $_3$ B $_8$ with Kagome-type iron framework. Dalton Trans 2016;45:9590–600. https://doi.org/10.1039/C6DT01164K.

[16] Hoyer E. V. I. Matkovich (Hrsg.). Boron and Refractory Borides. Springer-Verlag, Berlin, Heidelberg, New York 1977. VIII + 656 S., 271 Abb., 120 Tab., Preis DM 180, - US $ 79,20. Krist Tech 1978;13:552–552. https://doi.org/10.1002/crat.19780130514.

[17] Rades S, Kornowski A, Weller H, Albert B. Wet-Chemical Synthesis of Nanoscale Iron Boride, XAFS Analysis and Crystallisation to α-FeB. ChemPhysChem 2011;12:1756–60. https://doi.org/10.1002/cphc.201001072.

[18] Abeysinghe JP, Kölln AF, Gillan EG. Rapid and Energetic Solid-State Metathesis Reactions for Iron, Cobalt, and Nickel Boride Formation and Their Investigation as Bifunctional Water Splitting Electrocatalysts. ACS Mater Au 2022;2:489–504. https://doi.org/10.1021/acsmaterialsau.1c00079.

[19] Coey JMD. Magnetism and magnetic materials. Cambridge: Cambridge University Press; 2010.

[20] Lewis LH, Jiménez-Villacorta F. Perspectives on Permanent Magnetic Materials for Energy Conversion and Power Generation. Metall Mater Trans A 2013;44:2–20. https://doi.org/10.1007/s11661-012-1278-2.

[21] Wuttig M, Deringer VL, Gonze X, Bichara C, Raty J-Y. Incipient Metals: Functional Materials with a Unique Bonding Mechanism. Adv Mater 2018;30:1803777. https://doi.org/10.1002/adma.201803777.

[22] Pathak R, Ahamed I, Zhang WY, Vallopilly S, Sellmyer DJ, Skomski R, et al. Half-metallic magnetism in Ti $_3$ Co $_{5-x}$ Fe $_x$ B $_2$. AIP Adv 2017;7:055713. https://doi.org/10.1063/1.4976302.

[23] Kuz'ma, Yu B., Ya P. Yarmolyuk. Crystal structure of the compound Ti3Co5B2. J Struct Chem 1971;12:422–4.

[24] Zhang Y, Miller GJ, Fokwa BPT. Computational Design of Rare-Earth-Free Magnets with the Ti3Co5B2-Type Structure. Chem Mater 2017;29:2535–41. https://doi.org/10.1021/acs.chemmater.6b04114.

[25] Shankhari P, Scheifers JP, Hermus M, Yubuta K, Fokwa BPT. Unexpected Trend Deviation in Isoelectronic Transition Metal Borides A3T5B2 (A = group 4, T = group 9): Ti3Co5B2- vs. Perovskite-Type Studied by Experiments and DFT Calculations. Z Für Anorg Allg Chem 2017;643:1551–6. https://doi.org/10.1002/zaac.201700271.

[26] Shankhari P, Bakshi NG, Zhang Y, Stekovic D, Itkis ME, Fokwa BPT. A Delicate Balance between Antiferromagnetism and Ferromagnetism: Theoretical and Experimental Studies of A2MRu5B2 (A=Zr, Hf; M=Fe, Mn) Metal Borides. Chem – Eur J 2020;26:1979–88. https://doi.org/10.1002/chem.201904572.

[27] Nagelschmitz EA, Jung W. Scandium Iridium Boride $Sc_3Ir_5B_2$ and the Quaternary Derivatives $Sc_2MIr_5B_2$ with M = Be, Al, Si, Ti, V, Cr, Mn, Fe, Co, Ni, Cu, Ga, or Ge: Preparation, Crystal Structure, and Physical Properties. Chem Mater 1998;10:3189–95. https://doi.org/10.1021/cm9802898.

[28] Shankhari P, Janka O, Pöttgen R, Fokwa BPT. Rare-Earth-Free Magnets: Enhancing Magnetic Anisotropy and Spin Exchange Toward High-TC Hf2MIr5B2 (M = Mn, Fe). J Am Chem Soc 2021;143:4205–12. https://doi.org/10.1021/jacs.0c10778.

Chapter 2:

Experimental Techniques and Computational Methods

In this chapter, details of starting materials, synthesis routes, characterization techniques processing and property measurements of the solid materials are provided.

2.1 Synthesis Techniques

2.1.1 Overview

When synthesizing solid materials, care must be taken to use stoichiometric quantities and high purity starting materials since it is usually not possible to purify a solid once formed. High temperatures are generally required, typically between 500-2000°C, which requires a large input of energy. The coordination of many solids is high, varying from 4-12, depending on the size or charge of the elements. In general, solids are not raised to their melting temperatures so that the reaction occurs in the solid state. Solid-state reactions can only take place at the interface of two solids, and once the surface layer has reacted, the reaction continues as the reactants diffuse from the bulk to the interface. Raising the temperature enables the reaction at the interface and the diffusion through the solid to be faster than at room temperatures; a rule of thumb suggests that a temperature of about two-thirds of the melting temperature of the solids gives a reasonable reaction time. In many cases, diffusion is the rate-limiting factor. Therefore, it's crucial to thoroughly grind the starting materials in a pestle and mortar to

give a uniform small particle size. This will achieve a small particle size and maximize the surface contact while minimizing the distance the reactants need to diffuse. By pelletizing the mixed powders with a die set and hydraulic press, the number of crystallite faces in direct contact with one another can also be improved.[1,2] The apparatus for synthesis of solid materials is displayed in Figure 1.

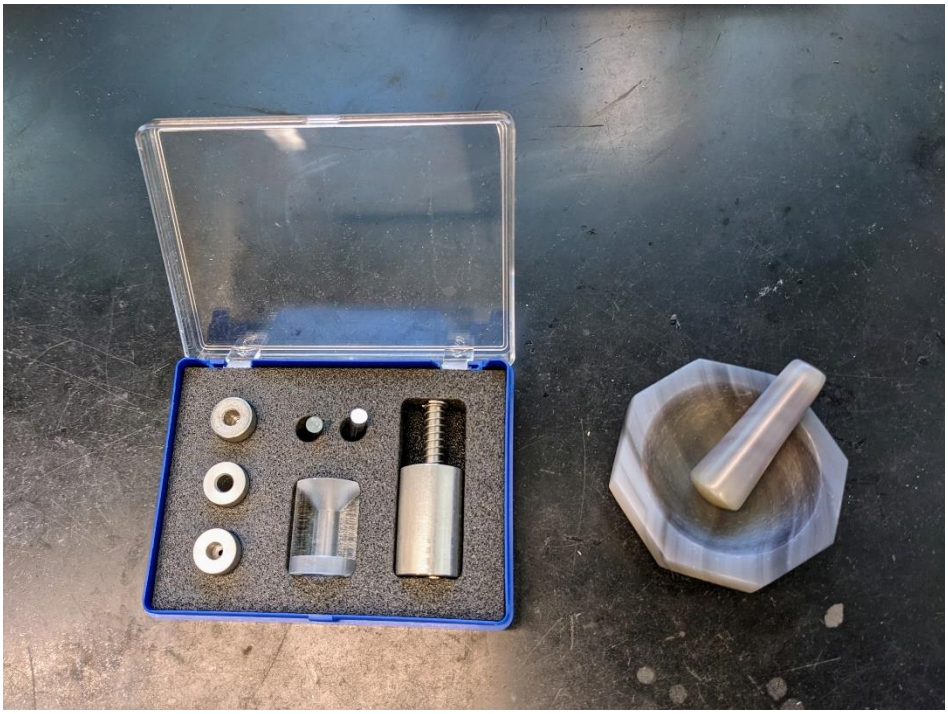

Figure 2.1: The basic apparatus for solid synthesis: (left) die set to pelletize powders and (right) pestle and mortar for fine grinding.

2.1.2 Sample Preparation

To prepare the samples for synthesis, commercially available high-purity elemental powders were used. The elements were then weighed according to the desired atomic ratio and pulverized in an agate mortar until homogeneous mixing was achieved.

Subsequently, the mixed powders were pressed into a pellet using a die-set (5-10 mm diameter) and a hydraulic press with a pressure ranging from 2-5 ton. All these procedures were performed inside a nitrogen glove box with an oxygen level below 2.0 ppm.

2.1.3 Arc Melting

As seen in Figure 2, the arc melting furnace consists of an encapsulated jar, a water-cooled copper crucible, an adjustable electrode (usually made of tungsten), and a direct current (DC) power supply. The sample is placed in the crucible, and the entire system is vacuumed to provide a clean environment inside. The chamber is vacuumed and purged with argon several times before melting to prevent oxidation. Before use, the argon gas is purified by passing it over silica gel, molecular sieves, and a titanium sponge. A high current flow generates an arc (ionized species in the jar) from the tungsten electrode, through the sample, passing through the copper, and returning to the DC power supply. The pellet is melted with a current ranging from 20-40 Amps, depending on the sample, for a few seconds. Special care was taken when using elements with low boiling points, as prolonged melting could cause these metals to evaporate.

Figure 2.2: Arc melting furnace used for experiments.

2.1.4 Tube Furnace

A tube furnace consists of a reaction chamber with a long cylinder where ampules are placed and heated. It allows for a region of controlled temperature to be maintained throughout a desired process, as seen in Figure 3. To synthesize using a tube furnace, the sample is first placed inside a closed-end quartz tube with a 10 mm inner diameter. The tube is vacuumed and purged with argon a few times before being vacuum-sealed. Afterwards, the sealed quartz tube is transferred to a tube furnace and subjected to the desired temperature profile for synthesis or annealing.

Figure 2.3: Vertical tube furnace used for experiments.

2.2 Characterization Techniques

2.2.1 Overview

X-ray diffraction is probably the most employed technique in solid-state inorganic chemistry and has many uses, from analysis and assessing the phase purity, to determining the structure. As seen in Figure 4a, an electrically heated filament, usually tungsten, emits electrons that are accelerated by a high potential difference (20–50 kV) and allowed to strike a metal target or an anode that is water-cooled. The anode emits a continuous spectrum of ‘white’ X-radiation, but superimposed on this are sharp, intense

X-ray peaks (Kα, Kβ), as shown in Figure 4b. The frequencies of the Kα and Kβ lines are characteristic of the anode metal; the target metals most used in X-ray crystallographic studies are copper and molybdenum. These lines occur because the bombarding electrons knock out electrons from the innermost K shell (n = 1) and this in turn creates vacancies which are filled by electrons descending from the shells above. The decrease in energy appears as radiation; electrons descending from the L shell (n = 2) give the Kα lines, and electrons from the M shell (n = 3) give the Kβ lines. Normally, in X-ray diffraction, monochromatic radiation (a single wavelength or a very narrow range of wavelengths) is required. Usually, the Kα line is selected and the Kβ line is filtered out by using a filter made of a thin metal foil of the element adjacent (Z − 1) in the periodic table. Crystalline solids consist of regular arrays of atoms, ions, or molecules. Because of the periodic nature of the internal structure, it is possible for crystals to act as a three-dimensional diffraction grating to light. Only at specific orientations of the crystal with respect to the source and detector are X-rays ‘reflected’ from the planes. The reflection occurs only when the conditions for constructive interference are fulfilled.[1,3]

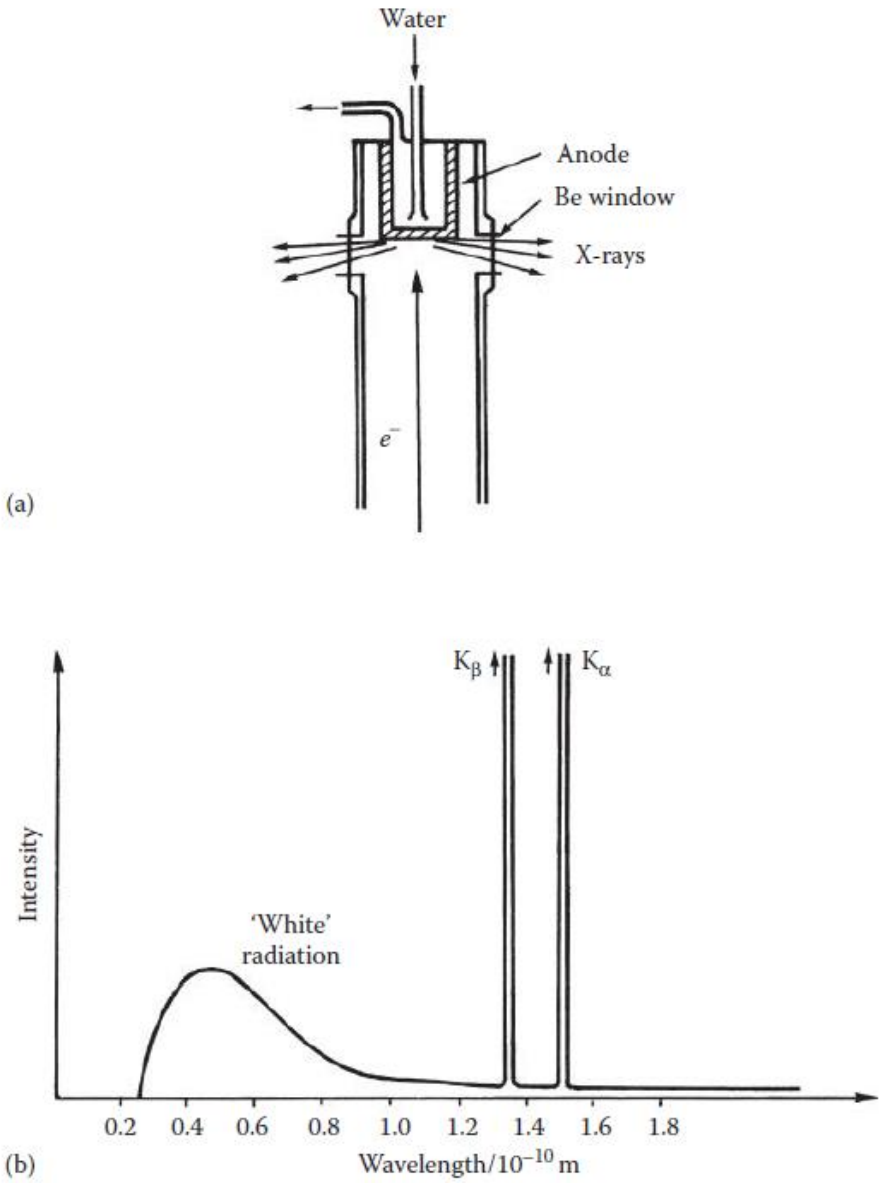

Figure 2.4: (a) Section through an X-ray tube. (b) An X-ray emission spectrum (reproduced from [1]).

2.2.2 Powder XRD Characterization

Powdered samples were subjected to X-ray diffraction analysis at room temperature using a Rigaku MiniFlex 600 diffractometer equipped with Cu-Kα radiation (λ = 1.54059 Å), image plate detector, and a Ge monochromator with silicon as the standard. This confirms the synthesis of phases and the crystallinity of the material. To ensure precise data, different step sizes and times were employed for the measurements. Subsequently, the FULLPROF program was used for phase analysis through the Rietveld refinement technique.[4,5]

2.2.3 Single-Crystal XRD Characterization

Single crystals suitable for analysis were extracted from the samples and analyzed using a Rigaku XtalLAB mini diffractometer with a wavelength of λ(Cu-Kα1) = 1.54059 Å. The intensities were adjusted for absorption using a numerical procedure based on Gaussian integration over a multifaceted crystal model found in the CrysAlis Pro package.[6] The data generated were interpreted and refined with SHELX employed by WinGX to obtain the final crystal structure.[7,8] This gives detailed information about the unit cell dimensions, bond lengths, and bond angles of crystalline substances. The metal atom positions were obtained using direct methods, while the boron position was determined by analyzing the electron density map after several full-matrix least-squares refinements (based on F^2).

2.2.4 Physical Property Measurement System

The magnetic measurements of crystalline powder $Hf_2Fe_{1-\delta}Ir_{5-x+\delta}Ru_xB_2$ were measured by utilizing a Vibrating Sample Magnetometer in an EverCool-II cryogen-free upgraded version of a Physical Property Measurement System (Quantum Design International, USA). Zero Field Cooling measurements were taken under different fields in the temperature range of 4 to 350 K after cooling in zero field. Field dependencies were measured between +4 and -4 T at various temperatures.

A different instrument was loaded with powders of $Ti_2FeOs_3B_3$ in polyethylene capsules. These were affixed to the rod of a Vibrating Sample Magnetometer (VSM) to quantify the magnetization M (T, H). Measurements were conducted via a Quantum Design Physical Property Measurement.

2.3 Computational Methods

2.3.1 Overview

Developing new materials based on existing structure types through elemental substitutions or intercalation of species is a promising avenue of research. The advancement of computational methods, particularly density functional theory (DFT), enables accurate calculations of thermodynamic stability and atomic interactions of complex solids. By screening hypothetical phases derived from a known structure type,

DFT calculations can greatly facilitate the synthesis of new stable compounds with desired properties.[9,10] Materials with diverse structures and compositions, such as metal borides, are particularly promising candidates. One study was conducted on the dependence of valence electrons (VE) in $Sc_2FeRu_{5-x}Ir_xB_2$ (x = 0-5, VE = 60-65), revealing that increasing the number of VE initially led to a decrease in antiferromagnetic (AFM) interactions between 60 to 62 VE. However, a transition from antiferromagnetism to ferromagnetism occurred between 62 and 63 VE, with further addition of valence electrons enhancing ferromagnetic (FM) interactions. The study found that Ru-rich quaternary phases (with less than 63 VE) exhibited dominating AFM interactions, while the Ir-rich phases (with more than 63 VE) were dominated by FM interactions.[11] Through the interpretation of their atomic interactions and the calculation of their stabilities, researchers can identify and design materials with tailored properties.

The density functional theory (DFT) is a powerful method for the simulation of chemical systems. It's built around the premise that the energy of an electronic system can be defined in terms of its electron probability density, ρ. For a system comprising n electrons, $\rho(r)$ represents the total electron density at a particular point in space r. The electronic energy E is regarded as a functional of the electron density $E[\rho]$, in the sense that to a given function $\rho(r)$ corresponds a single energy, i.e., a one-to-one correspondence between the electron density of a system and its energy exists. Generalized gradient approximation methods (GGAs), sometimes credited as nonlocal methods, have followed two main lines. One is more empirical in nature and is based on numerical fitting procedures involving large molecular training sets. These functionals

render particularly accurate atomization energies and reaction barriers for molecules but aren't successful in solid-state physics. The second group is more rational-based and considers that the development of exchange-correlation functionals should be anchored in basic principles derived from quantum mechanics, including scaling relations and the fulfillment of exact regions on the exchange and correlation holes. The exchange functionals based on this method include Becke (B86), Perdew (P), and Perdew-Burke-Ernzerhof (PBE). [12,13] All VASP calculations employed the generalized gradient approximation (GGA) with exchange and correlation treated by the Perdew-Burke-Enzerhoff (PBE) functionals.

2.3.2 VASP Calculations

DFT was applied to screen stability and magnetic interactions of different hypothetical ternary and quaternary compounds. This was done by calculating the total energy and electronic structures using VASP. Relative energies of different magnetic models were then analyzed.

The INCAR file is the central input file of VASP, which uses specified parameters to steer the calculations. The tags specified in the INCAR file select the algorithms and set the parameters that VASP uses during the calculation. The INCAR file is a tagged format free-ASCII file, meaning each statement follows a *tag = values* syntax. The POSCAR file specifies the periodic simulation cell and gives information regarding geometry of the system. VASP comes with a library of PAW datasets for elements of the

periodic table. The POTCAR file is the pseudopotential file and contains the PAW datasets for all atomic types specified in the POSCAR file. The KPONTS file specifies the points VASP will use to sample the first Brillouin zone in reciprocal space. [14,15]

Figure 5 depicts a sample INCAR file. ISTART starts the job, with ISTART=1 being a continuation job. It is the usual setting for convergence tests with respect to the cut-off energy for all jobs where the volume or cell-shape varies. ICHARG determines how VASP constructs the initial charge density. ICHARG=11 will obtain the eigenvalues or the density of states of a given charge density read from CHGCAR. PREC defines the precision of the calculation, with PREC=accurate reducing egg-box effects and errors the most. ISMEAR determines how the partial occupancies are set for each orbital, and ISMEAR=-5 is the tetrahedron method with Blöchl corrections. EDIFF is the convergence criteria for the energy in units of eV. The relaxation of the electronic degrees of freedom stops if the total energy change and the band-structure-energy change between two steps are both smaller than EDIFF. ENCUT specifies the cutoff energy for the plane wave basis in eV. [14]

```
#Computational settings

LPLANE=.FALSE. #switches on the plane-wise data distribution in real space. TRUE., the data distributio
NCORE=4 #determines determines the number of compute cores that work on an individual orbital.
LSCALU=.FALSE. #switches on the parallel LU decomposition (using scaLAPACK) in the orthonormalization o
NSIM=4 #NSIM sets the number of bands that are optimized simultaneously by the RMM-DIIS algorithm.

#Initialization
#GGA=RP #Determines which GGA DFT funnctional we want to use. RP=RPBE, RE=revPBE ,B3/B5=B3LYP.
ALGO=VeryFast #Determines which algorithm is used to optimize orbitals. Similar to ALGO=normal, Fast, o
#IALGO=38 #=38 same as normal or fast ALGO
ISTART=1 # 1 read WAVECAR if it exists
ICHARG=11 # determines how VASP constructs the initial charge density. 11 to read from an available CHG
LAECHG=.TRUE. #the all-electron charge density will be reconstructed explicitly and written out to file
LCHARG=.TRUE. #Determines whether the charge densities are recorded in CHGCAR and CHG.
PREC=accurate #specifies the "precision"-mode
#ISYM=0 #Switches off the use of symmetry except psi=its complex conjugate. =-1 switches it off complet

#Electronic Optimization

ISPIN=2
ISMEAR=-5 #determines how the partial occupancies fnk are set for each orbital. SIGMA determines the wi
SIGMA=0.1 #specifies the width of the smearing in eV. By combining ISPIN with MAGMOM collinear magnetis
LREAL=AUTO #determines whether the projection operators are evaluated in real-space or in reciprocal sp
NELM=200 #sets the maximum number of electronic SC (selfconsistency) steps which may be performed.
NELMIN=5 #specifies the minimum number of electronic SCF steps. Ideally between 4-8.
EDIFF=1E-06 #global break condition for the electronic SC-loop. Convergence criteria.
ENCUT=450.00 #specifies the cutoff energy for the planewave basis set in eV. should be ~1-1.3x of large
```

Figure 2.5: Example INCAR file.

References:

[1] Elaine A. Moore, Lesley E. Smart. Solid State Chemistry: An Introduction. 4th Edition. CRC Press; 2012.

[2] Chamorro JR, McQueen TM. Progress toward Solid State Synthesis by Design. Acc Chem Res 2018;51:2918–25. https://doi.org/10.1021/acs.accounts.8b00382.

[3] Harris KDM, Tremayne M, Kariuki BM. Contemporary Advances in the Use of Powder X-Ray Diffraction for Structure Determination. Angew Chem Int Ed 2001;40:1626–51. https://doi.org/10.1002/1521-3773(20010504)40:9<1626::AID-ANIE16260>3.0.CO;2-7.

[4] Rodríguez-Carvajal J. AN INTRODUCTION TO THE PROGRAM n.d.

[5] Young RA. The Rietveld Method. Oxford University Press; 1995.

[6] Rigaku Oxford Diffraction. CrysAlisPro Software system, version 1.171.38.46. Oxford, UK: Rigaku Corporation; 2018.

[7] Sheldrick GM. A short history of SHELX. Acta Crystallogr A 2008;64:112–22. https://doi.org/10.1107/S0108767307043930.

[8] Farrugia LJ. *WinGX* and *ORTEP for Windows* : an update. J Appl Crystallogr 2012;45:849–54. https://doi.org/10.1107/S0021889812029111.

[9] Park CW, Wolverton C. Developing an improved crystal graph convolutional neural network framework for accelerated materials discovery. Phys Rev Mater 2020;4:063801. https://doi.org/10.1103/PhysRevMaterials.4.063801.

[10] Saal JE, Kirklin S, Aykol M, Meredig B, Wolverton C. Materials Design and Discovery with High-Throughput Density Functional Theory: The Open Quantum Materials Database (OQMD). JOM 2013;65:1501–9. https://doi.org/10.1007/s11837-013-0755-4.

[11] Hermus M, Yang M, Grüner D, DiSalvo FJ, Fokwa BPT. Drastic Change of Magnetic Interactions and Hysteresis through Site-Preferential Ru/Ir Substitution in $Sc_2FeRu_{5-x}Ir_xB_2$. Chem Mater 2014;26:1967–74. https://doi.org/10.1021/cm500237h.

[12] Sousa SF, Fernandes PA, Ramos MJ. General Performance of Density Functionals. J Phys Chem A 2007;111:10439–52. https://doi.org/10.1021/jp0734474.

[13] Orio M, Pantazis DA, Neese F. Density functional theory. Photosynth Res 2009;102:443–53. https://doi.org/10.1007/s11120-009-9404-8.

[14] Georg Kresse, Jurgen Furthmuller. Vienna Ab initio Simulation Package 2005.

[15] Hafner J. Materials simulations using VASP—a quantum perspective to materials science. Comput Phys Commun 2007;177:6–13. https://doi.org/10.1016/j.cpc.2007.02.045.

Chapter 3:

Role of Hafnium and Magnetic Characteristics in Quinary System $Hf_2Fe_{1-\delta}Ir_{5-x+\delta}Ru_xB_2$

Diana Luong, Sam Kilic, Elena Haddon, Boniface P. T. Fokwa

3.1 Abstract

Structural and magnetic characteristics of new quinary members of the Hf-series, $Hf_2Fe_{1-\delta}Ir_{5-x+\delta}Ru_xB_2$ (x = 1-4, VE = 63-66), have been investigated. They were synthesized via arc-melting and characterized by powder and single-crystal X-ray diffraction. Theoretical calculations using DFT indicate a preference for magnetic ordering in all compounds but with a strong competition between ferro- and antiferromagnetism. The spin exchange and magnetic anisotropy energies were evaluated, and they predicted intrinsic semi-hard to hard magnetic behaviors. The magnetization measurements demonstrate the presence of both antiferromagnetic and ferromagnetic interactions in all compounds, with coercivities ranging between 0.134 and 3.94 kA/m^{-1} at 5 K, suggesting soft to semi-hard behaviors. Surprisingly, all members except one exhibit a notable hysteresis at room temperature. A significant difference in magnetic interactions is found between the 5d Hf and the 3d Sc and Ti that have been used in previous and similar series, suggesting a potential magnetic tuning using these non-magnetic elements in the future.

3.2 Introduction

Due to boron's ability to gain and lose electrons, it can form a rich tapestry of compounds. Metal borides can have covalent B-B bonds, ionic M-B bonds, and even metallic M-M/M-B bonds. For metal-rich borides, isolated boron atoms are surrounded by a metal atom. With increasing boron content, strong covalent B-B bonds form, producing one-dimensional boron chains, zigzags, two-dimensional sheets, and eventually progressing to three-dimensional boron networks. These variations give rise to several exciting physiochemical properties such as high melting point, strong hardness, extraordinary magnetic properties, and remarkable chemical inertness.[1–5] With an abundant variety of crystal structures, these compounds can be used in numerous industrial applications such as permanent magnets ($Nd_2Fe_{14}B$)[6,7], superconductors (MgB_2)[8,9], and conductive ceramics (HfB_2)[10]. Metal borides are thus potential candidates for various other applications in electronics, catalysis, ion transport, and sensing.

One versatile structure type within the metal-rich boride family, $Ti_3Co_5B_2$ (space group *P*4/*mbm*, no. 127), which includes ternaries (with general composition $A_3T_5B_2$), quaternaries ($A_2MT_5B_2$), and quinaries [$A_2M(TT')_5B_2$], has more than seventy known compounds to date and has provided some exotic magnetic properties.[4] The ternary variant is composed of face-sharing trigonal, tetragonal, and pentagonal prisms of T atoms (electron-rich transition metals such as Co, Rh, Ir). The A atoms (larger transition or main group elements such as Mg, Sc, Ti) reside in the tetragonal and pentagonal

prisms whereas the smaller boron atoms are located within the trigonal prisms. Of special interest are the quaternary variants containing a magnetic element M such as Fe, Mn, Co that occupy the tetragonal prisms and form chains of M atoms along [001].[11–14] Intrachain M-M distance of approximately 3.1 Å allows for direct magnetic interactions whereas the interchain distance of approximately 6.5 Å allows for indirect interactions mediated by conduction electrons. These unique features attributes to long-range magnetic ordering such as antiferromagnetism in $Sc_2FeRu_5B_2$, ferromagnetism in $Sc_2FeRh_5B_2$,[15] and metamagnetism in $Sc_2FeIr_5B_2$.[16]

In a valence electron (VE) dependence study of $Sc_2FeRu_{5-x}Ir_xB_2$ (x = 0-5, VE = 60-65), it was realized that increasing the number of VE first resulted in decreased antiferromagnetic (AFM) interactions from 60 to 62 VE. A transition from antiferromagnetism to ferromagnetism occurred between 62 and 63 VE. Adding more valence electrons enhanced the ferromagnetic (FM) interactions. This study demonstrated that Ru-rich quaternary phases (with less than 63 VE) displayed dominating AFM interactions whereas the Ir-rich phases (with more than 63 VE) were dominated by FM interactions.[17] Similar results were obtained for other VE-dependent studies such as $Sc_2FeRu_{5-x}Rh_xB_2$[18] and $Ti_2FeRu_{5-x}Rh_xB_2$.[19] A new quaternary boride, $Hf_2FeIr_5B_2$ (67 VE), was synthesized recently in our group which maximized the number of 5d elements and valence electron count. Strong FM interactions occurred between the Fe intrachains and the interchains, leading to a high ordering temperature of T_C = 900 K and coercivity H_c = 12.1 kA/m. Most importantly, this new phase exhibited hysteresis above room temperature, a prerequisite for a future application as permanent magnetic material .[20]

This current work focuses on new quinary members of this Hf-series, $Hf_2Fe_{1-\delta}Ir_{5-x+\delta}Ru_xB_2$ (x = 0-5, VE = 62-67), detailing the magnetic characteristics as a function of valence electron count and the role of the 5d hafnium as compared to the 3d Sc and Ti.

3.3 Experimental Method

Quinary members of the series $Hf_2Fe_{1-\delta}Ir_{5-x+\delta}Ru_xB_2$ were synthesized via the starting elementals: hafnium (powder, 99.6% Alfa Aesar), iron (powder, 99% Alfa Aesar), iridium (powder, 99.9% Alfa Aesar), ruthenium (powder, 99.9% Alfa Aesar), and boron (amorphous powder, 97% Alfa Aesar). They were weighed in their respective atomic ratios, mixed, and pelletized inside a glovebox. The pellet was transferred to an arc-melting furnace with a water-cooled copper crucible connected to a Schlenk line. Melting was executed under an argon atmosphere with a tungsten tip as a second electrode until homogeneous melting was acquired. The argon was purified prior to use over silica gel, molecular sieves, and titanium sponge (950 K). The result were bulk samples with a silver metallic luster, giving several single crystals suitable for X-ray structure analysis. All phases were air stable as compact bulk as well as finely ground powders. Sample preparation and handling were performed using an agate mortar and pestle and tungsten carbide die sets to avoid contamination.

3.4 Computational Method

All VASP calculations employed the generalized gradient approximation (GGA) with the Perdew-Burke-Enzerhoff (PBE) functionals.[21] The cutoff energy for the plane wave calculations was set to 450 eV and the Brillouin zone integrations were carried out using a 7 x 7 x 19 k-point mesh for all compounds.

3.5 Results and Discussion

The overall features of $Hf_2Fe_{1-\delta}Ir_{5-x+\delta}Ru_xB_2$ are the same as those of the quaternary $Hf_2FeIr_5B_2$: all samples crystallize in the tetragonal system with the space group *P*4/*mbm*. As seen in Figure 1, the structural building units are composed of edge-sharing Ru/Ir chains, forming trigonal prisms where boron reside, quaternary prisms where iron reside, and pentagonal prisms where hafnium reside.

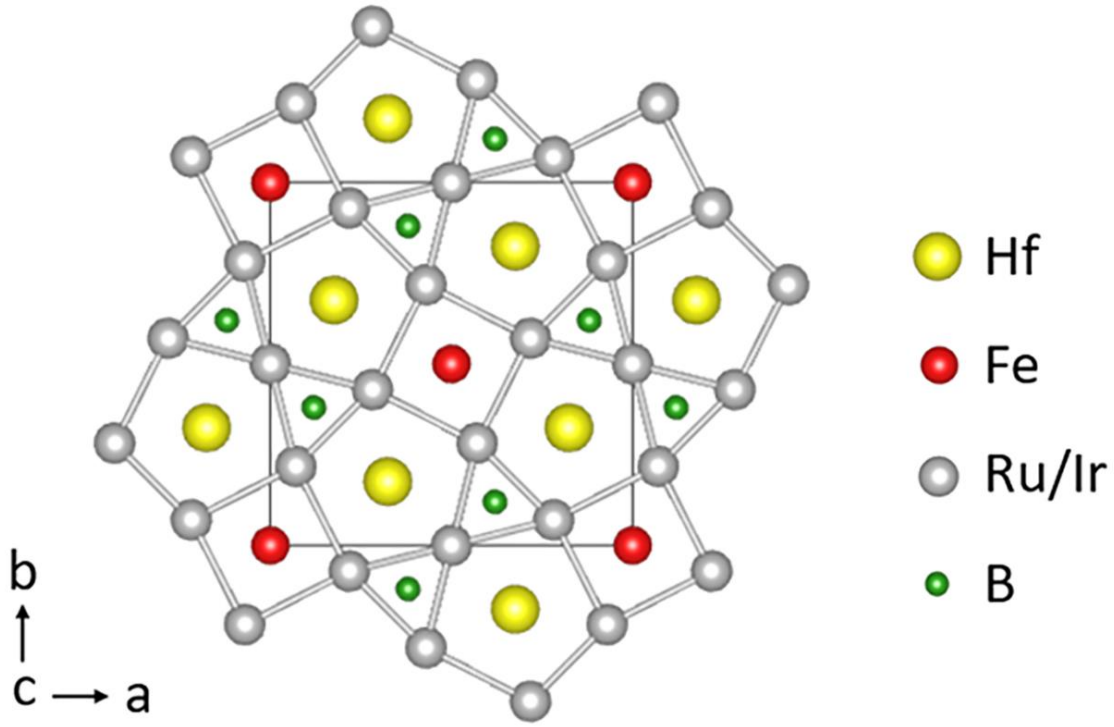

Figure 3.1. Crystal structure of $Hf_2Fe_{1-\delta}Ir_{5-x+\delta}Ru_xB_2$ viewed along [001].

Characterization was conducted by powder X-ray diffraction (PXRD) and single crystal X-ray diffraction (SCXRD). The quinary members of the $Hf_2Fe_{1-\delta}Ir_{5-x+\delta}Ru_xB_2$ series were the main phase and could be assigned to the $Ti_3Co_5B_2$ structure type. A secondary phase, $HfIr_3B_{0.5}$, appeared in the Ir-rich phases with an amount of approximately 8%. In the Ru-rich phases, there is also a small quantity of a secondary phase, but it could not be identified. Rietveld refinement obtained using the FullProf suite are depicted in Figure 2, with agreement seen between the observed (red) and the calculated (black) lines. The difference pattern (blue) line and Bragg (green) lines are displayed at the bottom. The starting space group, lattice parameters, and atomic positions for the Rietveld refinement were fitted using the $Sc_2FeRu_{5-x}Ir_xB_2$ series by

Hermus et al.,[17] swapping out scandium with hafnium. Structural parameters and profile parameters from the refinement results are detailed in Table 1.

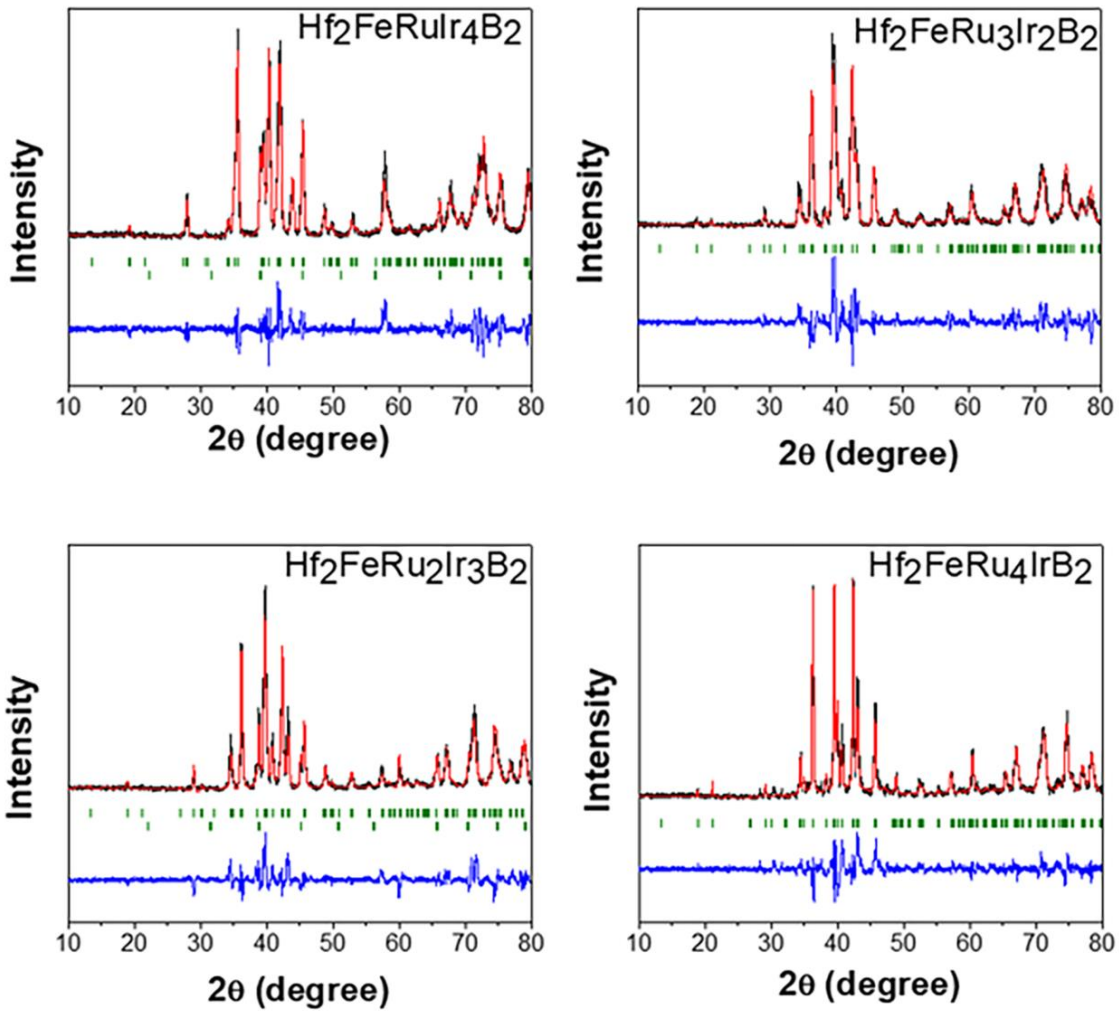

Figure 3.2. Rietveld refinements of the powder XRD samples for $Hf_2Fe_{1-\delta}Ir_{5-x+\delta}Ru_xB_2$. The red curve is the measured pattern, the black curve is the calculated pattern, and the blue curve is the intensity difference. Bragg peak positions are displayed in green.

Table 3.1. Rietveld Refinement of $Hf_2Fe_{1-\delta}Ir_{5-x+\delta}Ru_xB_2$.

Formula	$Hf_2FeRuIr_4B_2$	$Hf_2FeRu_2Ir_3B_2$	$Hf_2FeRu_3Ir_2B_2$	$Hf_2FeRu_4IrB_2$	$Hf_2FeRu_5B_2$
Space Group	P 4/m b m				
a (Å)	9.2156(3)	9.3565(3)	9.4015(3)	9.3936(2)	9.3779(4)
b (Å)	9.2156(3)	9.3565(3)	9.4015(3)	9.3936(2)	9.3779(4)
c (Å)	3.1887(1)	3.0806(1)	3.0621(2)	3.0630(1)	3.0760(2)
Unit cell volume ($Å^3$)	270.80(2)	269.69(2)	270.65(2)	270.28(1)	270.51(2)
Formula units per cell	2				
Calculated density (g/cm^3)	15.677	19.536	14.501	13.607	11.643
2θ range	10.02-79.96				
Refinement Range	Least-squares				
Profile Function	Pseudo-voigt				
R_{Bragg}	6.81	11.2	10.3	9.53	16.0
R_F	4.59	6.80	5.65	6.22	9.79
R factors	R_P = 11.5	R_P = 13.8	R_P = 14.3	R_P = 12.2	R_P = 19.3
	R_{WP} = 14.8	R_{WP} = 17.7	R_{WP} = 18.2	R_{WP} = 15.5	R_{WP} = 24.0
χ^2	4.14	6.03	7.23	5.02	1.54

Single-crystal data and structure refinement of $Hf_2Fe_{1-\delta}Ir_{5-x+\delta}Ru_xB_2$ are shown in Table 2. All refinements converged to reasonably small R factors. The goodness of fit for all single crystals was approximately 1.2 with R_1 values (all data) of up to 8.11% and wR_2 values of up to 17.71%, indicating acceptable refinement. The electron density difference ranged at most from 7.27 to -6.56, but were located around the heavy elements Ru, Hf, and Ir. This even distribution verifies that all electrons were accounted for in the

structures. The site occupancies and isotropic thermal parameters are given in Table 3. Iridium preference is revealed towards the 8i site and ruthenium preference towards the 2d site, resembling the scandium series, $Sc_2FeIr_{5-x}Ru_xB_2$. One difference in the ruthenium-rich phases is that iridium would occupy the iron 2b site at nearly the same ratio as the 8i site. SCXRD shows $Hf_2FeRu_4IrB_2$ with Ir site occupancy factor (*sof*) of 0.343 in the 2b site while in $Hf_2FeRu_3Ir_2B_2$ it has a *sof* of 0.424. No iridium was found occupying the iron site in the scandium series. Once the iridium content surpasses fifty percent, a sharp rise of Ir is found in the 8i site. The occupation of the iron 2b site by iridium also roughly vanishes for the Ir-rich samples.

Table 3.2. Atomic and thermal parameters of $Hf_2Fe_{1-\delta}Ir_{5-x+\delta}Ru_xB_2$.

Atom	Site	x	y	z	sof
$Hf_2FeRu_{3.66(2)}Ir_{1.34(2)}B_2$					
Ru1	2d	0.5	0	0	0.90(2)
Ir1	2d	0.5	0	0	0.10(2)
Ru2	8i	0.2180(2)	-0.0705(2)	0	0.69(2)
Ir2	8i	0.2180(2)	-0.0705(2)	0	0.31(2)
Hf1	4h	0.3241(1)	0.1759(1)	0.5	1.00
Fe3	2b	0	0	-0.5	0.66(2)
Ir3	2b	0	0	-0.5	0.34(2)
B1	4h	0.620(3)	0.120(3)	-0.5	1.00
$Hf_2FeRu_{2.98(2)}Ir_{2.02(2)}B_2$					
Ru1	2d	0.5	0	0	0.86(2)
Ir1	2d	0.5	0	0	0.14(2)
Ru2	8i	0.2182(2)	-0.0705(2)	0	0.53(2)

Ir2	8i	0.2182(2)	-0.0705(2)	0	0.47(2)
Hf1	4h	0.3240(2)	0.1760(2)	0.5	1.00
Fe3	2b	0	0	-0.5	0.58(2)
Ir3	2b	0	0	-0.5	0.42(2)
B1	4h	0.623(4)	0.123(4)	-0.5	1.00
$Hf_2FeRu_{1.68(2)}Ir_{3.32(2)}B_2$					
Ru1	2d	0.5	0	0	0.60(2)
Ir1	2d	0.5	0	0	0.40(2)
Ru2	8i	0.2159(8)	-0.0705(7)	0	0.28(1)
Ir2	8i	0.2159(8)	-0.0705(7)	0	0.73(1)
Hf1	4h	0.3242(7)	0.1758(7)	0.5	1.000
Fe3	2b	0	0	-0.5	1.000
B1	4h	0.623(2)	0.123(2)	-0.5	1.000
$Hf_2FeRu_{1.36(2)}Ir_{3.64(2)}B_2$					
Ru1	2d	0.5	0	0	0.77(2)
Ir1	2d	0.5	0	0	0.24(2)
Ru2	8i	0.2172(8)	-0.0691(8)	0	0.15(2)
Ir2	8i	0.2172(8)	-0.0691(8)	0	0.85(2)
Hf1	4h	0.3244(8)	0.1756(8)	0.5	1.00
Fe3	2b	0	0	-0.5	0.95(2)
Ir3	2b	0	0	-0.5	0.05(2)
B1	4h	0.616(2)	0.116(2)	-0.5	1.00

Table 3.3. Single-crystal data and structure refinement of $Hf_2Fe_{1-\delta}Ir_{5-x+\delta}Ru_xB_2$.

Refined composition	$Hf_2FeRu_{3.66(2)}Ir_{1.34(2)}B_2$	$Hf_2FeRu_{2.98(2)}Ir_{2.02(2)}B_2$	$Hf_2FeRu_{1.68(2)}Ir_{3.32(2)}B_2$	$Hf_2FeRu_{1.36(2)}Ir_{3.64(2)}B_2$
Valence electrons	63.34(2)	64.02(2)	65.32(2)	65.32(2)
Formula weight (g/mol)	1030.93	1122.06	1213.19	1304.32
Crystal size (mm^3)	0.06 x 0.08 x 0.09	0.05 x 0.06 x 0.08	0.07 x 0.09 x 0.09	0.01 x 0.12 x 0.19
a (Å)	9.394(2)	9.146(2)	9.2711(7)	9.2528(4)
b (Å)	9.394(2)	9.146(2)	9.2711(7)	9.2528(4)
c (Å)	3.0565(7)	2.978(2)	3.1240(3)	3.1650(4)
Volume ($Å^3$)	269.7(2)	249.1(2)	268.52(5)	270.97(4)
Calculated density (g/cm^3)	6.347	7.479	7.502	7.993

Abs. coefficient (mm^{-1})	38.097	53.075	60.213	70.541
θ range (deg)	3.067-33.512	3.150-33.132	3.107-33.084	3.114-33.360
hkl range	h = -13 → 14 k = -14 → 14 l = -4 → 4	h = -14 → 12 k = -13 → 13 l = -4 → 4	h = -11 → 13 k = -13 → 12 l = -4 → 4	h = -14 → 13 k = -14 → 13 l = -4 → 4
Total reflections	1907	1975	2398	4058
Unique reflections	328	299	296	325
Number parameters	21	21	21	21
R_1/wR_2	0.0811/0.1125	0.0793/0.1771	0.0399/0.0797	0.0502/0.1075
Goodness-of-fit	1.283	1.124	1.134	1.222

Plots of lattice parameters and cell volume as a function of valence electrons are depicted in Figure 3. The refined lattice parameters, a = 9.3779(4) Å and c = 3.0760(2) Å for $Hf_2FeRu_5B_2$, gradually increases in the a-lattice while decreasing in the c-lattice until it reaches 64 VE $Hf_2FeIr_2Ru_3B_2$ (a = 9.4015(3) Å and c = 3.0621(2) Å). At the Ir-rich phase $Hf_2FeIr_3Ru_2B_2$ of 65 VE, the trend changes to a-lattice decreasing sharply while the c-lattice increases with iridium addition all the way to 67 VE $Hf_2FeIr_5B_2$ (a = 9.0975(7) Å and c = 3.2040(3) Å). This behavior is characteristic of the $Ti_3Co_5B_2$ structure-type series[18,19,22]. This also follows the trend of the similar quinary series $Sc_2FeIr_{5-x}Ru_xB_2$, where a-lattice expansion and c-lattice contraction continued until 64 VE before shifting to a-lattice shrinking and c-lattice increasing. The main difference in the Hf-series is that there is modest Ir occupancy in the 2b iron site for the ruthenium-rich phases. Upon reaching the Ir-rich phase $Hf_2FeIr_3Ru_2B_2$ at 65 VE, the trend changes to a-lattice shrinking while the c-lattice expands. At this stage, the 8i site becomes dominated by iridium atoms, with less preference towards the 2d site and nearly none in the 2b site. Due to the opposite variations of a and c, a nearly consistent volume is achieved across all intermediate phases.

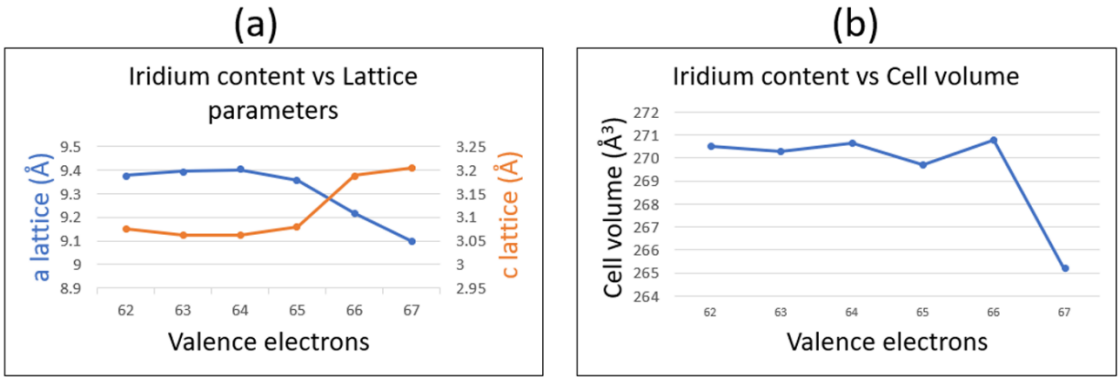

Figure 3.3. Lattice parameters (a) and cell volume (b) as a function of valence electrons.

3.6 Theoretical Calculations

DFT calculations were used to investigate the stability and spin orientations of the new compounds. Total energies of FM, AFM, and nonmagnetic (NM) models were calculated to determine the lowest ground state. Single-crystal X-ray diffraction data was used to create structural models for the calculations and determine where best to place atoms. The 2b site could be incorporated with either iron or iridium, however iridium content never surpassed 0.5 sof for any of the single crystal data. Not only that, but iridium atoms had little to no occupancy in the 2b site in the iridium-rich phases of the series. This led to the conclusion that the models should have iron occupancy only at the 2b site. The 2d site could consist of either ruthenium or iridium. However, in all single crystals, ruthenium always prevailed at that location. Thus, that site was kept as ruthenium for every model. For the 8i site, while keeping the ratios in accordance with the stoichiometry, ruthenium and iridium were randomly distributed amongst the eight sites. Figure 4 depicts the most stable configurations of $Hf_2Fe_{1-\delta}Ir_{5-x+\delta}Ru_xB_2$. The FM

model has both iron FM intrachain and interchain interactions. The AFM model has iron FM intrachain interactions while interchain interactions are AFM. Table 4 displays the relative energies with respect to the most stable model. In the ruthenium-rich phases, the AFM model is the most stable, whereas in the iridium-rich phases, the FM model is the most stable. All magnetic models were more stable than the nonmagnetic one by over 1500 meV, indicating preference for magnetic ordering. Consistent with the computational study previously conducted,[23] all models of this same structure type exhibited a preference for some form of magnetic ordering. In the case of $Zr_2FeRu_5B_2$ and $Hf_2FeRu_5B_2$, these compounds favored interchain Fe-Fe AFM interactions, as expected based on their VE of 62.

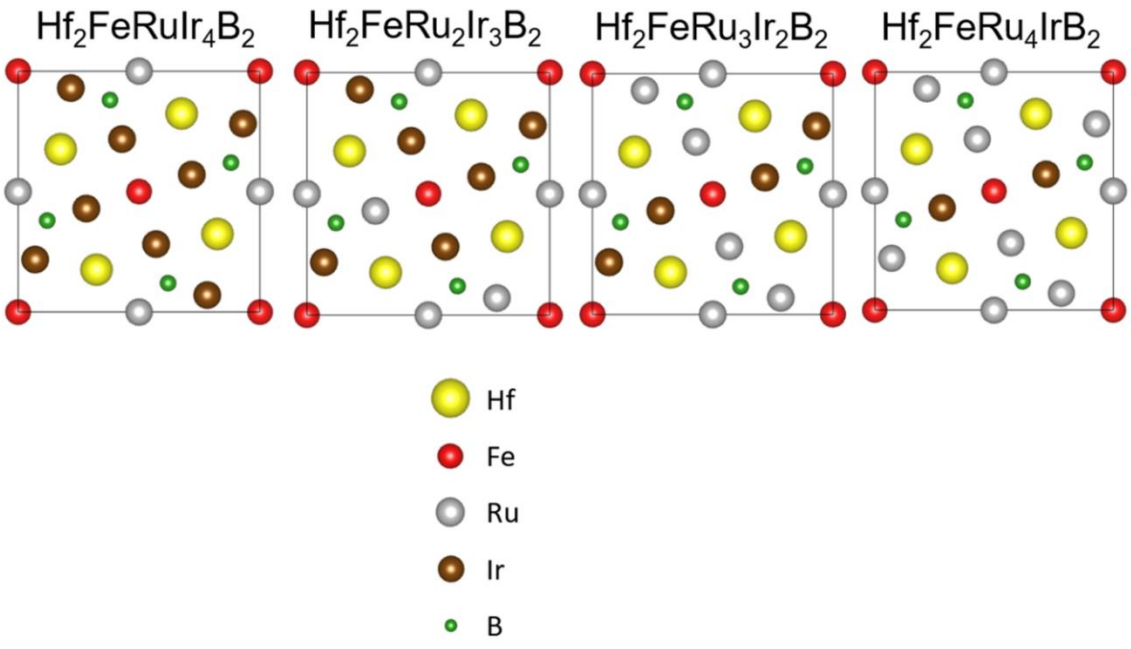

Figure 3.4. Most stable ground state configurations of $Hf_2Fe_{1-d}Ir_{5-x+d}Ru_xB_2$.

Table 3.4. Relative energies of different magnetic models for $Hf_2Fe_{1-\delta}Ir_{5-x+\delta}Ru_xB_2$.

Compound	FM (meV)	AFM (meV)	NM (meV)
$Hf_2FeRu_1Ir_4B_2$	0	+32.885	+2255.107
$Hf_2FeRu_2Ir_3B_2$	0	+15.293	+2207.412
$Hf_2FeRu_3Ir_2B_2$	+24.694	0	+2032.338
$Hf_2FeRu_4Ir_1B_2$	+779.533	0	+1724.540

The nonspin-polarized (nsp) and spin-polarized of (sp) density of states (DOS) of all new quinaries are illustrated in Figure 5 and 6, respectively. All nsp DOS is at high states at the Fermi level (E_F), indicating electronic instability. These states all decrease significantly in the spin-polarized (sp) calculations, pointing to electronic stabilization of these compounds and preference for magnetic ordering. Quaternaries $Zr_2MnRu_5B_2$ and $Hf_2FeRu_5B_2$ calculated previously also displayed a decrease in the number of states at E_F when comparing sp vs the nsp DOS, agreeing with this trend. Zr and Hf revealed no states at E_F in the partial nsp DOS, while Mn and Fe exhibited significant states at E_F, signifying the magnetic elements as the source of electronic instability.[23] Since Fe contributes the majority number of states to E_F, it is reasonable to infer that Fe is primarily responsible for the instability observed in the quinaries.

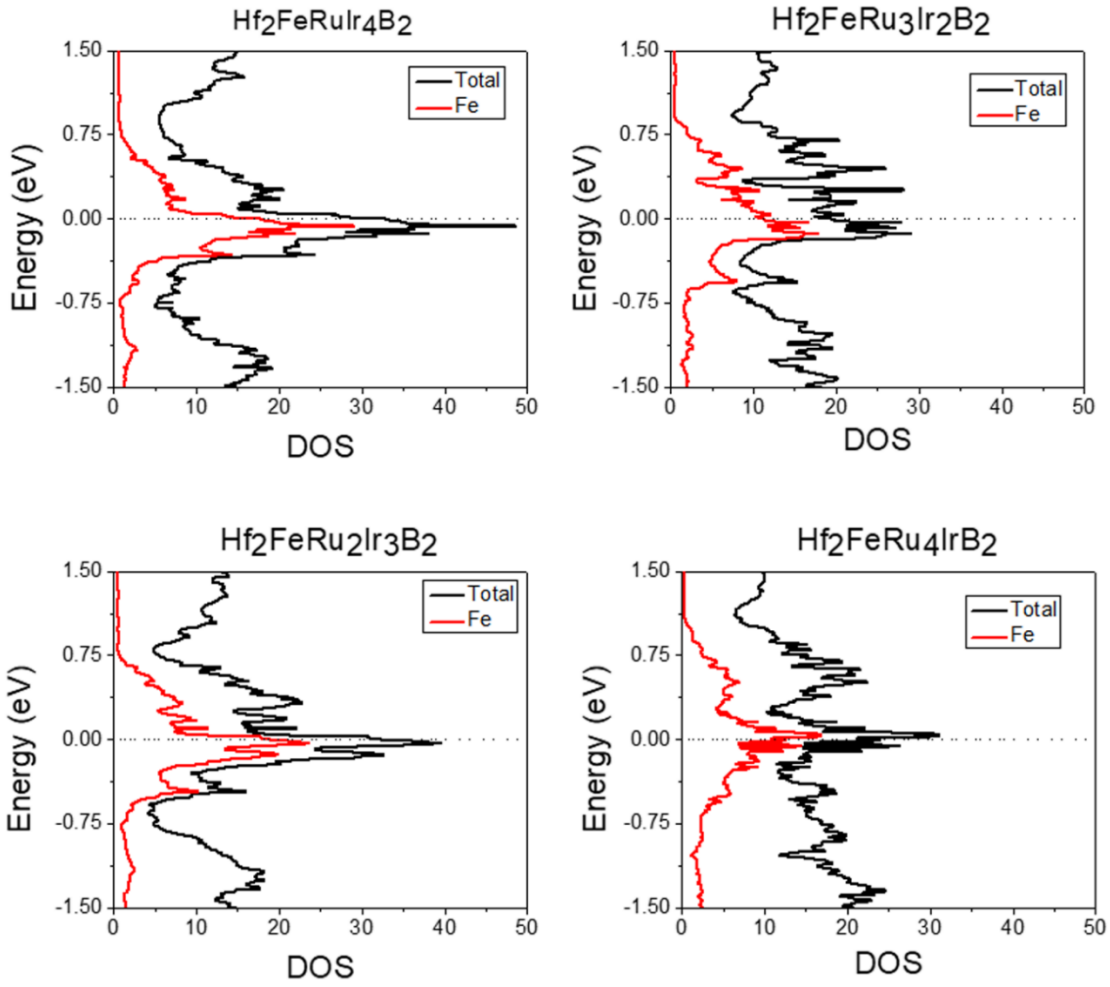

Figure 3.5. Non-spin polarized Density of States (DOS) for series $Hf_2Fe_{1-\delta}Ir_{5-x+\delta}Ru_xB_2$.

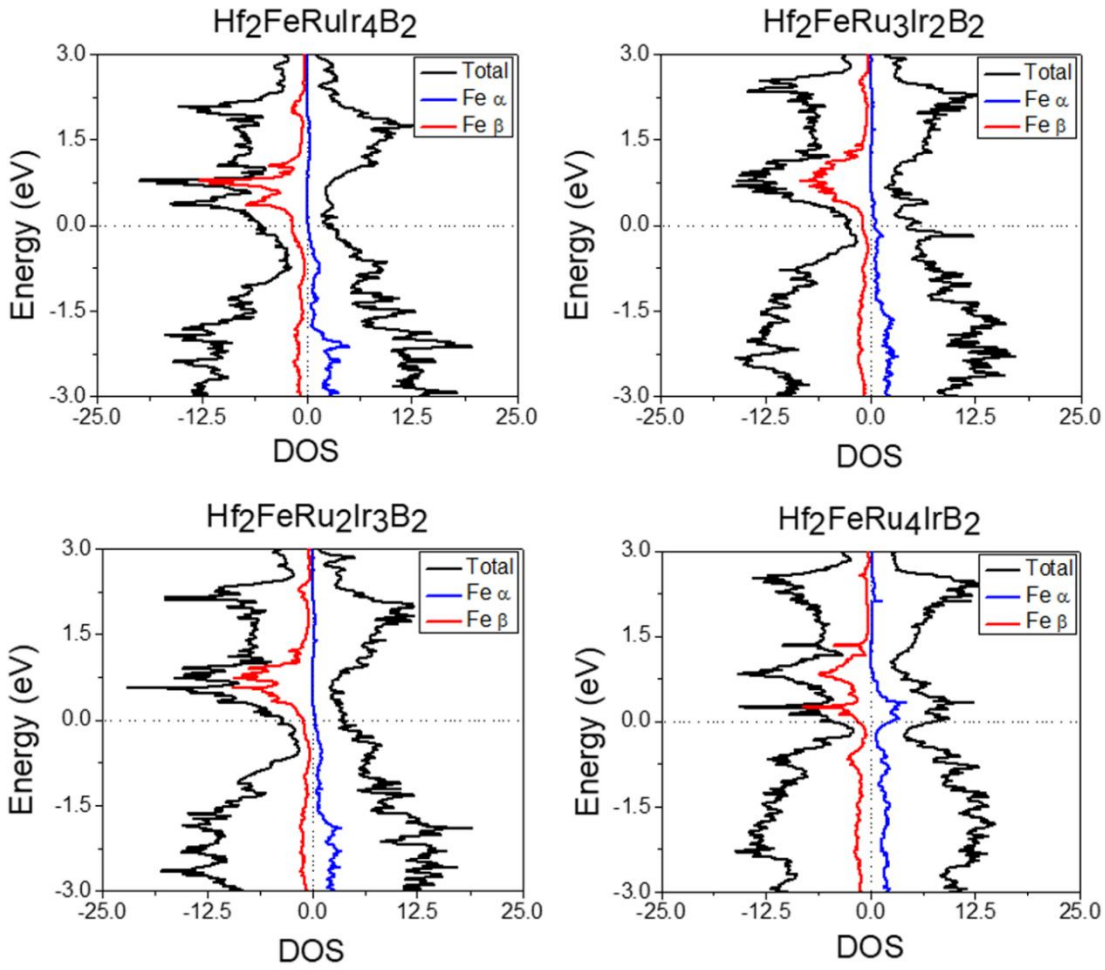

Figure 3.6. Spin polarized Density of States (DOS) for series $Hf_2Fe_{1-\delta}Ir_{5-x+\delta}Ru_xB_2$.

The spin exchange energy is the phenomenon where individual magnetic moments will attempt to align within a material. If magnetic moments align parallel, the material is ferromagnetic; if the moments align antiparallel, the material is antiferromagnetic. This energy is estimated from the difference between the FM and AFM spin orientations.[20] From the VASP calculations, the Ru-rich series prefer AFM ordering while the Ir-rich series prefer FM ordering. The resulting VASP energies for

spin exchange and spin-orbit-coupling are given in Table 3 along with each compounds' valence electron count. The presence of strong interchain spin exchange interactions between Fe atoms makes it harder to flip the spins of isolated Fe chains when subjected to an external magnetic field, resulting in higher coercivity. Thus, high spin exchange refers to a strong interaction between spins, with $Hf_2FeRu_4Ir_1B_2$ being the greatest at -389.77 meV/f.u. followed by $Hf_2FeRu_5B_2$ at -62.26 meV/f.u.

To be practical, these materials also need a large magnetic anisotropy energy (MAE), which originates from the spin-orbit coupling (SOC) effect. Two factors contribute to the total E_{MAE}: (i) the single-element magnetic anisotropy energy (E_{SOC}), which is influenced by SOC, and (ii) the long-range magnetic dipole−dipole (MDD) interaction energy (E_{MDD}). E_{MDD} makes relatively very small contributions to E_{MAE} compared with SOC, and thus the net E_{SOC} is approximately equal to E_{MAE}.[24,25] The total energy difference between magnetization parallel to the c-axis (∥c) and perpendicular to the c-axis (⊥c) is defined as MAE, i.e.,

$$E_{MAE} \approx E_{SOC} = E(\|c) - E(\perp c)$$

For each compound, total energies of spin parallel ($E_{SOC} \parallel c$) and spin perpendicular ($E_{SOC} \perp c$) to the crystallographic c-axis were calculated. The calculated energies indicate that the easy axis is the (001) direction from 62-65 VE, and it switches to the (100) direction from 66-67 VE. As displayed in Table 3, $Hf_2FeIr_5B_2$ has the highest E_{SOC} at

+3.27 meV/f.u.[20] followed by $Hf_2FeRuIr_4B_2$ at +2.92 meV/f.u. These two have large MAE arising from the Ir-Fe coupling along the a-axis.

Table 3.5. Exchange Energy E_{EX} ($E_{AFM} - E_{FM}$), Spin Orbit Coupling Energy E_{SOC} ($E_{SOC} \parallel c - E_{SOC} \perp c$), and VE of $Hf_2Fe_{1-\delta}Ir_{5-x+\delta}Ru_xB_2$.

Compound	E_{EX} (meV/f.u.)	E_{SOC} (meV/f.u.)	VE
$Hf_2FeRu_5B_2$	-62.26	-0.39	62
$Hf_2FeRu_4IrB_2$	-389.77	-0.03	63
$Hf_2FeRu_3Ir_2B_2$	-12.35	-1.46	64
$Hf_2FeRu_2Ir_3B_2$	+7.65	-0.39	65
$Hf_2FeRuIr_4B_2$	+16.44	+2.92	66
$Hf_2FeIr_5B_2$	+40.19	+3.27	67

Overall, significant spin exchange interactions and MAE, particularly influenced by the strong SOC effect, are essential requirements for achieving high coercivity and robust magnetic anisotropy in materials of the $Ti_3Co_5B_2$-type. Comparing both E_{EX} and E_{SOC}, the best magnet candidate would be $Hf_2FeIr_5B_2$. It has the highest E_{SOC} +3.27 meV/f.u. paired with an exchange energy E_{EX} of +40.19 meV/f.u.[20] Even though $Hf_2FeRu_4IrB_2$ has the strongest exchange energy, it has the lowest E_{SOC} of -0.033 meV/f.u., meaning the electron spins are oriented very weakly along the easy axis c. Of

the newly-synthesized intermediates, $Hf_2FeRuIr_4B_2$ would be the best magnet candidate since it has the second highest E_{SOC} at +2.92 meV/f.u. coupled with E_{EX} of +16.44 meV/f.u. Most hard magnetic materials that are rare-earth-free have much smaller E_{SOC} values, such as MnBi with E_{SOC} of -0.15 meV/f.u., making these new quinaries relatively strong. Another notable compound is $Hf_2MnIr_5B_2$, which has the third highest E_{EX} (-60.01 meV/f.u.) and the fourth highest E_{SOC} (-1.55 meV/f.u.).[20] The series $Sc_2FeRu_{5-x}Ir_xB_2$, specifically the members with 62 and 63 VE, displayed intrinsic H_c values of up to 52.4 kA/m but at a temperature of 5 K. $Sc_2FeRu_3Ir_2B_2$ has the seventh highest E_{EX} of -36.77 meV/f.u. but is coupled with the third highest E_{SOC} of -2.83 meV/f.u. The calculated E_{EX} revealed the coexistence of competing FM and AFM interactions, with AFM interactions prevailing and leading to a significantly low magnetization (0.45 μB/f.u.) in this compound.[13] To be applicable, the ordering temperatures and E_{MAE} need to be still improved.

3.7 Magnetic Results and Discussion

Magnetization measurements against temperature under zero-field cooling (ZFC) and field cooling (FC) were executed to investigate the magnetic properties of $Hf_2FeIr_{5-x}Ru_xB_2$. The ZFC and FC magnetization-temperature curves are presented in Figure 7. Due to limitations of the PPMS-VSM device, measurements were performed at a 1000 Oe applied magnetic field from a temperature range of 4 – 350 K, which was not beyond the transition temperature of the products. Samples were initially cooled from 300 K

down to 4 K in the absence of a magnetic field for the ZFC curve. A field of 1000 Oe was then applied, and measurements were made in the warming cycle. FC experimental curves were attained by cooling from 350 K down to 4 K while maintaining a constant applied field at 1000 Oe and magnetization measurements were recorded as a function of increasing temperature. In all the quinaries, irreversibility in magnetization is visible with a peak in the ZFC curve. All samples show an AFM transition, with $Hf_2FeRuIr_4B_2$ having the highest Neel temperature at approximately 75 K. However, the broad peak represents weak antiferromatic interactions and there may be other competing factors in play. $Hf_2FeRu_3Ir_2B_2$ would have the strongest antiferromagnetic interactions as it displays the sharpest peak amongst all the quinaries. The presence of an unknown side phase mentioned earlier is neglected in the interpretation of magnetic data; therefore, interpretations may be inaccurate. Figure S4 illustrates the magnetic susceptibility χ^{-1} against temperature T. The available data is insufficient for a discussion on the Curie-Weiss constant.

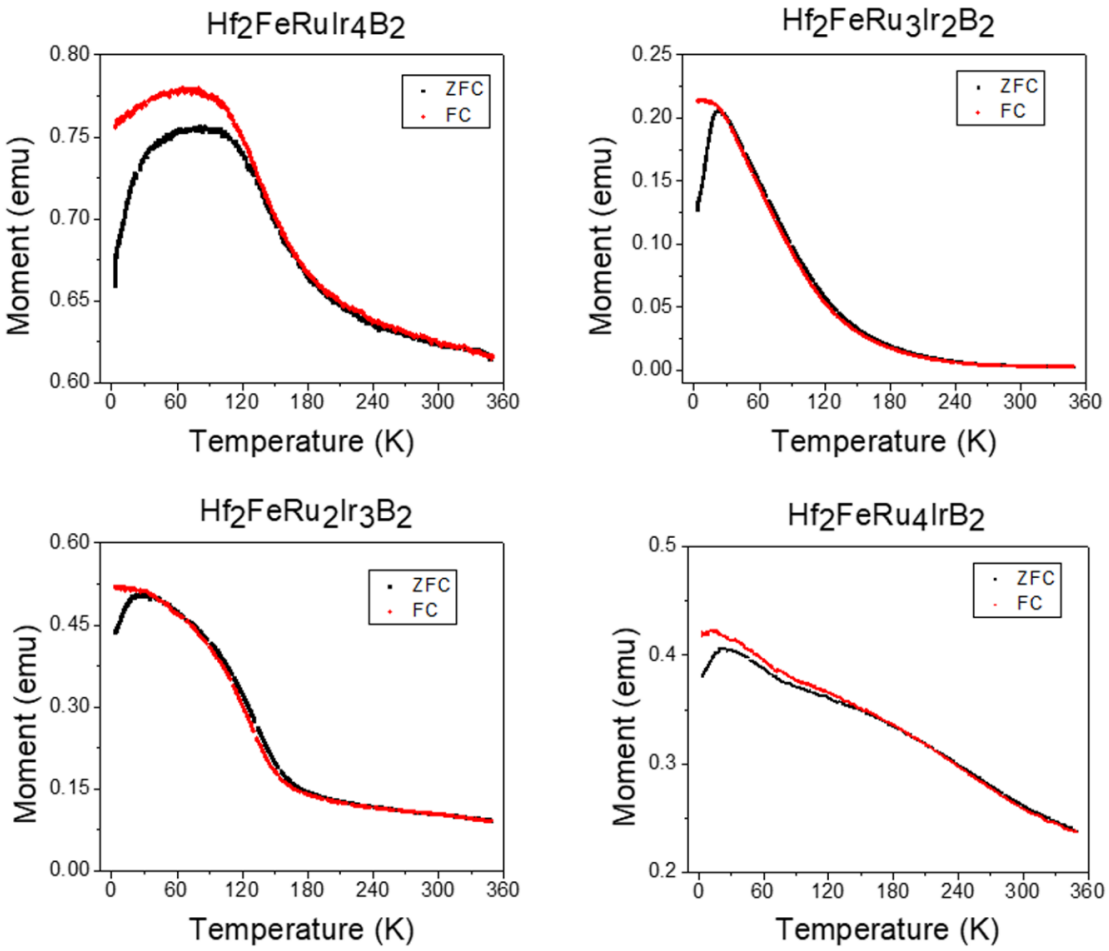

Figure 3.7. ZFC/FC magnetization curves of $Hf_2Fe_{1-\delta}Ir_{5-x+\delta}Ru_xB_2$ measured at 1000 Oe.

Magnetization curves measured at 300 K are displayed in figure 8. Magnetic coercivity stands out as a crucial parameter that impacts the suitability of this novel group of materials. No saturation magnetization was reached at room temperature. Calculated magnetic moments are displayed in Table S2, revealing $Hf_2FeRu_2Ir_3B_2$ with the highest moment at 3.082 emu. $Hf_2FeRu_4IrB_2$ had the weakest calculated moment of 2.793 emu, which was observed only for one iron atom. The second iron atom had a negligible

moment (0.014 emu) and thus is not contributing significantly to the overall magnetic behavior. Nevertheless, $Hf_2FeRu_4IrB_2$ has a notable Curie temperature since the measured magnetic moment remains relatively high. The key characteristic that defines soft magnets is a low coercivity (H_c < 1 kAm^{-1}). Soft magnetic materials reach saturation magnetization when exposed to a relatively weak magnetic field, and they demagnetize and switch polarity when subjected to a relatively weak magnetic field with opposite polarity. $Hf_2FeRu_4IrB_2$ has the lowest H_c at 0.134 kAm^{-1}, and this value increases as more iridium is introduced. However, at $Hf_2FeRuIr_4B_2$, H_c suddenly drops to 0.508 kAm^{-1} before increasing again. Both $Hf_2FeRu_4IrB_2$ and $Hf_2FeRuIr_4B_2$ would be classified as soft magnets, whereas $Hf_2FeRu_3Ir_2B_2$ and $Hf_2FeRu_2Ir_3B_2$ would fall into the semi-hard category. However, these are intrinsic hardness properties, thus they can be further improved by synthetic means with the aim of enhancing the extrinsic properties through microstructure engineering, as has been demonstrated for BiMn.[26] The series $Sc_2FeIr_{5-x}Ru_xB_2$ exhibits the same characteristic: $Sc_2FeRu_4IrB_2$ has the lowest H_c at 13.5 kAm^{-1}. As the amount of iridium increases, there is a rise in atomic magnetic dipole moment and coercivity. At the iridium-rich phase, $Sc_2FeRuIr_4B_2$, stronger ferromagnetic interactions exist, but coercivity reaches its minimum value at H_c = 0.4 kAm^{-1}.[17] Table S3 shows the comparison of coercivity obtained from the hysteresis loops at 5 K for series $Hf_2Fe_{1-\delta}Ir_{5-x+\delta}Ru_xB_2$ and $Sc_2FeRu_{5-x}Ir_xB_2$.The introduction of scandium creates a distinction in that $Sc_2FeRu_2Ir_3B_2$ and $Sc_2FeRu_3Ir_2B_2$ is able to achieve a hard magnet (H_c > 30 kAm^{-1}). In the series $Ti_2FeRu_{5-n}Rh_nB_2$, there's a general trend of coercivity decreasing with

increasing electron count.[19] With no 5d metal incorporated, this series has a completely different pattern from other transition metal borides.

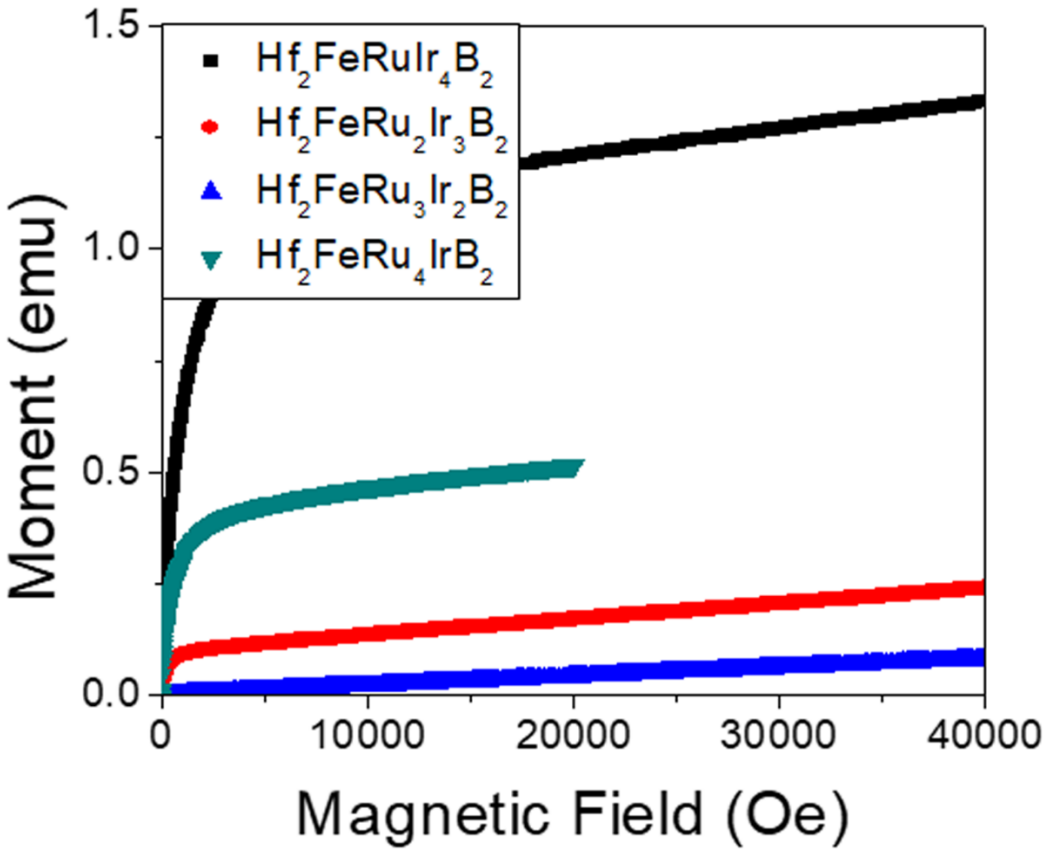

Figure 3.8. Magnetization curves measured at 300 K of series $Hf_2Fe_{1-\delta}Ir_{5-x+\delta}Ru_xB_2$.

3.8 Conclusion

In this study, we investigated the magnetic characteristics of the new quinary series $Hf_2Fe_{1-\delta}Ir_{5-x+\delta}Ru_xB_2$. Characterization using PXRD and SCXRD confirmed the synthesis of the compounds. The magnetic properties were investigated using DFT calculations, which showed a preference for magnetic ordering in all compounds.

$Hf_2FeRuIr_4B_2$ demonstrated the highest MAE and exchange energy among the quinaries. Magnetization measurements revealed antiferromagnetic transitions in all compounds, with $Hf_2FeRuIr_4B_2$ exhibiting the highest Neel temperature. The coercive fields were relatively low, indicating the soft magnet nature of $Hf_2FeRu_4IrB_2$ and $Hf_2FeRuIr_4B_2$, while $Hf_2FeRu_3Ir_2B_2$ and $Hf_2FeRu_2Ir_3B_2$ exhibited semi-hard magnet characteristics. These novel materials show potential for various applications in magnetoelectronics and warrant further exploration and optimization.

References

[1] Yang X, Ding Y, Ni J. *Ab initio* prediction of stable boron sheets and boron nanotubes: Structure, stability, and electronic properties. Phys Rev B 2008;77:041402. https://doi.org/10.1103/PhysRevB.77.041402.

[2] Albert B, Hillebrecht H. Boron: Elementary Challenge for Experimenters and Theoreticians. Angew Chem Int Ed 2009;48:8640–68. https://doi.org/10.1002/anie.200903246.

[3] Dronskowski R, Kikkawa S, Stein A. Handbook of Solid State Chemistry, 6 Volume Set. John Wiley & Sons; 2017.

[4] Scheifers JP, Zhang Y, Fokwa BPT. Boron: Enabling Exciting Metal-Rich Structures and Magnetic Properties. Acc Chem Res 2017;50:2317–25. https://doi.org/10.1021/acs.accounts.7b00268.

[5] Kondo T. Recent progress in boron nanomaterials. Sci Technol Adv Mater 2017;18:780–804. https://doi.org/10.1080/14686996.2017.1379856.

[6] Givord, D., H. S. Li, J. M. Moreau. Magnetic properties and crystal structure of Nd2Fe14B. Solid State Commun 1984;50:497–9.

[7] Kramer MJ, Lewis LH, Fabietti LM, Tang Y, Miller W, Dennis KW, et al. Solidification, microstructural refinement and magnetism in Nd2Fe14B. J Magn Magn Mater 2002;241:144–55. https://doi.org/10.1016/S0304-8853(01)00955-6.

[8] Jones ME, Marsh RE. The Preparation and Structure of Magnesium Boride, MgB_2. J Am Chem Soc 1954;76:1434–6. https://doi.org/10.1021/ja01634a089.

[9] Buzea C, Yamashita T. Review of the superconducting properties of MgB_2. Supercond Sci Technol 2001;14:R115–46. https://doi.org/10.1088/0953-2048/14/11/201.

[10] Chen L, Gu Y, Shi L, Yang Z, Ma J, Qian Y. Synthesis and oxidation of nanocrystalline HfB2. J Alloys Compd 2004;368:353–6. https://doi.org/10.1016/j.jallcom.2003.08.086.

[11] Kuz'ma, Yu B., Ya P. Yarmolyuk. Crystal structure of the compound Ti3Co5B2. J Struct Chem 1971;12:422–4.

[12] Shankhari P, Scheifers JP, Hermus M, Yubuta K, Fokwa BPT. Unexpected Trend Deviation in Isoelectronic Transition Metal Borides A3T5B2 (A = group 4, T = group 9): Ti3Co5B2- vs. Perovskite-Type Studied by Experiments and DFT Calculations. Z Für Anorg Allg Chem 2017;643:1551–6. https://doi.org/10.1002/zaac.201700271.

[13] Zhang Y, Miller GJ, Fokwa BPT. Computational Design of Rare-Earth-Free Magnets with the Ti3Co5B2-Type Structure. Chem Mater 2017;29:2535–41. https://doi.org/10.1021/acs.chemmater.6b04114.

[14] Petermüller B, Neun C, Stekiel M, Zimmer D, Tribus M, Wurst K, et al. Synthesis, Crystal Structure, and Compressibilities of Mn3−xIr5B2+x (0≤x≤0.5) and Mn2IrB2. Chem – Eur J 2018;24:14679–85. https://doi.org/10.1002/chem.201803235.

[15] Samolyuk GD, Fokwa BPT, Dronskowski R, Miller GJ. Electronic structure, chemical bonding, and magnetic properties in the intermetallic series Sc 2 Fe (Ru 1 − x Rh x) 5 B 2 from first principles. Phys Rev B 2007;76:094404. https://doi.org/10.1103/PhysRevB.76.094404.

[16] Nagelschmitz EA, Jung W. Scandium Iridium Boride Sc $_3$ Ir $_5$ B $_2$ and the Quaternary Derivatives Sc $_2$ MIr $_5$ B $_2$ with M = Be, Al, Si, Ti, V, Cr, Mn, Fe, Co, Ni, Cu, Ga, or Ge: Preparation, Crystal Structure, and Physical Properties. Chem Mater 1998;10:3189–95. https://doi.org/10.1021/cm9802898.

[17] Hermus M, Yang M, Grüner D, DiSalvo FJ, Fokwa BPT. Drastic Change of Magnetic Interactions and Hysteresis through Site-Preferential Ru/Ir Substitution in Sc $_2$ FeRu $_{5-x}$ Ir $_x$ B $_2$. Chem Mater 2014;26:1967–74. https://doi.org/10.1021/cm500237h.

[18] Fokwa BPT, Lueken H, Dronskowski R. Rational Synthetic Tuning between Itinerant Antiferromagnetism and Ferromagnetism in the Complex Boride Series Sc2FeRu5−nRhnB2 (0≤n≤5). Chem – Eur J 2007;13:6040–6. https://doi.org/10.1002/chem.200700128.

[19] Fokwa BPT, Lueken H, Dronskowski R. Rational Design of Complex Borides – One-Electron-Step Evolution from Soft to Semi-Hard Itinerant Ferromagnets in the New Boride Series Ti2FeRu5–nRhnB2 (1 ≤ n ≤ 5). Eur J Inorg Chem 2011;2011:3926–30. https://doi.org/10.1002/ejic.201100315.

[20] Shankhari P, Janka O, Pöttgen R, Fokwa BPT. Rare-Earth-Free Magnets: Enhancing Magnetic Anisotropy and Spin Exchange Toward High-TC Hf2MIr5B2 (M = Mn, Fe). J Am Chem Soc 2021;143:4205–12. https://doi.org/10.1021/jacs.0c10778.

[21] Perdew JP, Burke K, Ernzerhof M. Generalized Gradient Approximation Made Simple. Phys Rev Lett 1996;77:3865–8. https://doi.org/10.1103/PhysRevLett.77.3865.

[22] Fokwa BPT, Hermus M. Complete Titanium Substitution by Boron in a Tetragonal Prism: Exploring the Complex Boride Series Ti $_{3-x}$ Ru $_{5-y}$ Ir $_y$ B $_{2+x}$ ($0 \le x \le 1$ and $1 < y < 3$) by Experiment and Theory. Inorg Chem 2011;50:3332–41. https://doi.org/10.1021/ic102148x.

[23] Shankhari P, Bakshi NG, Zhang Y, Stekovic D, Itkis ME, Fokwa BPT. A Delicate Balance between Antiferromagnetism and Ferromagnetism: Theoretical and Experimental Studies of A2MRu5B2 (A=Zr, Hf; M=Fe, Mn) Metal Borides. Chem – Eur J 2020;26:1979–88. https://doi.org/10.1002/chem.201904572.

[24] Błoński P, Hafner J. Magnetic anisotropy of transition-metal dimers: Density functional calculations. Phys Rev B 2009;79:224418. https://doi.org/10.1103/PhysRevB.79.224418.

[25] Koo H-J, Xiang H, Lee C, Whangbo M-H. Effect of Magnetic Dipole−Dipole Interactions on the Spin Orientation and Magnetic Ordering of the Spin-Ladder Compound $Sr_3Fe_2O_5$. Inorg Chem 2009;48:9051–3. https://doi.org/10.1021/ic9007526.

[26] Tang W, Ouyang G, Liu X, Wang J, Cui B, Cui J. Engineering microstructure to improve coercivity of bulk MnBi magnet. J Magn Magn Mater 2022;563:169912. https://doi.org/10.1016/j.jmmm.2022.169912.

Chapter 4:

Synthesis and Magnetic Properties of the Transition Metal-Rich Boride $Ti_2FeOs_3B_3$

Diana Luong, Michael Küpers, Rainer Pöttgen, Boniface P. T. Fokwa

4.1 Abstract

Transition metal-rich borides exhibit a diverse array of crystal structures and intriguing physical properties. These compounds are known for their magnetic behaviors, magnetocaloric effects, mechanical hardness, and superconductivity. $Ti_2FeOs_3B_3$, featuring B_4 zigzag fragments, iron dumbbell chains (Fe ladder), and osmium-rich, is synthesized and investigated for its magnetic properties. Theoretical calculations reveal the antiferromagnetic state as the most stable, however the sample exhibits strong attraction to an external magnetic field at room temperature. Magnetic measurements confirm an AFM transition at low temperatures, but the ferromagnetic state prevails under the influence of strong magnetic fields. The modest energy distinction (around 8 meV) between the expected AFM1 and FM magnetic ground states suggests that even minor modifications can shift the equilibrium. This work highlights the complex interplay between composition, bonding, and magnetic behavior in this compound.

4.2 Introduction

Transition metal-rich borides are of great interest due to their wide range of crystal structures and fascinating physical properties. Metal borides have exceptional physical behaviors such as magnetic and magnetocaloric properties, high mechanical hardness, and superconductivity.[1] The structural motifs in these compounds can be classified primarily by the ratio of metal to boron. In compounds with high metal to boron (M:B) ratios, such as in M_3B (M=Re, Tc) or $Ti_3Co_5B_2$ type structures[2,3], isolated boron atoms are often located at the center of a trigonal prism consisting of metal atoms (MB_6). At lower M:B ratios of around 2:1, a greater variety of boron fragments are formed as they start to connect to each other, including B_2 dumbbells, B_4 or B_5 chains, trigonal planar fragments, or B_6 rings.[4,5] In these cases, metal atoms form an arrangement of trigonal prisms that are connected by a shared rectangular face and allows boron to form covalent B-B bonds. At even lower M:B ratios, the presence of boron layers and three-dimensional networks arises. These different boron fragments forming with metals allows for a fragment-based approach to these crystal systems.

Many M:B combinations have been reported, such as $Re_5Co_2B_4$ (isolated B and B_2 dumbbells)[6], $Ti_7Rh_4Ir_2B_8$ (isolated B and B_6 rings)[7], and $Ti_{1+x}Rh_{2-x+y}Ir_{3-y}B_3$ (isolated B and zig-zag B_4 chains.[8] These boron fragments were also found to interact with chains of magnetic 3d elements (Cr, Fe) to produce new phases showing interesting magnetic ordering phenomena. For example, ferromagnetism was observed for B_6/Fe-chain combination in $Nb_6Fe_{1-x}Ir_{6+x}B_8$[9] and for trigonal-planar B_4/Fe_3-chain combination in

$TiFe_{1-x}Os_{2+x}B_2$[10], while ferrimagnetism was found for trigonal-planar B_4/Cr_3-chain combination in $TiCrIr_2B_2$.[11] Another B_4/Fe_2-chain combination was reported for the $Ti_2Fe_{0.91(1)}Ir_{3.09(1)}B_3$ ($Ti_{1+x}Rh_{2-x+y}Ir_{3-y}B_3$-type) phase[8], but no magnetic ordering was found, and it was speculated that the Fe_2-chain interacting with a different B_4 fragment (zigzag) might be responsible. Nevertheless, the element composition and overall valence electron count could significantly influence its properties, thus studying other compounds of the same structure type would help in comprehending this behavior and uncovering new magnetic materials. This optimism is routed in previous reports of Fe_2-chain (Fe-ladder) producing $Ti_9Fe_2Ru_{18}B_8$[12] ferromagnet, albeit without boron in the vicinity of the Fe_2-chain.

Herein, we report on the synthesis and magnetic properties of $Ti_2FeOs_3B_3$, an orthorhombic crystal with isolated B and zigzag B-chains. Starting with the model $Ti_2Fe_{0.91(1)}Ir_{3.09(1)}B_3$ reported by Dr. C. Görens[13], iridium was replaced by osmium leading to the discovery of a new Os-based compound with the same structure type.

4.3 Experimental Method

$Ti_2FeOs_3B_3$ was synthesized by first weighing out elemental Ti (powder, 99.5% Alfa Aesar), Fe (powder, 99% Alfa Aesar), Os (powder, 99.8% Thermo Scientific), and B (amorphous powder, 97% Alfa Aesar) in their stoichiometric ratios with a total mass of 0.25g. They were then grinded and compacted into pellets before being subjected to arc melting using a current of 40 A in a water-cooled copper crucible. This was performed

under an argon atmosphere with a tungsten tip as a second electrode. Prior to use, the argon gas underwent purification using silica gel, molecular sieves, and Ti sponge (heated to 950 K). After melting until homogeneous, a silver, metallic product was obtained.

4.4 Computational Method

DFT calculations were performed using the generalized gradient approximation (GGA) with the Perdew-Burke-Enzerhoff (PBE) functionals.[14] Total energies were calculated using the Monkhorst-Pack mesh[15] of k-points in the Brillouin zone with k-point mesh 7 x 3 x 13. The plane wave cut-off energy was 450 eV, and the total energy convergence criterion was set to 10^{-7} eV/cell.

4.5 Results and Discussion

The X-ray powder diffractogram shows a phase with the $Ti_{1+x}Rh_{2-x+y}Ir_{3-y}B_3$-type structure as the main component. The starting model for the Rietveld refinement of this new phase was $Ti_2FeOs_3B_3$, which possesses an orthorhombic structure with space group *Pbam*. Illustrated in Figure 1, a top-down view of the crystal shows it consists of both isolated boron atoms and zigzag chains. Iron dumbbells are found between the boron zigzags.

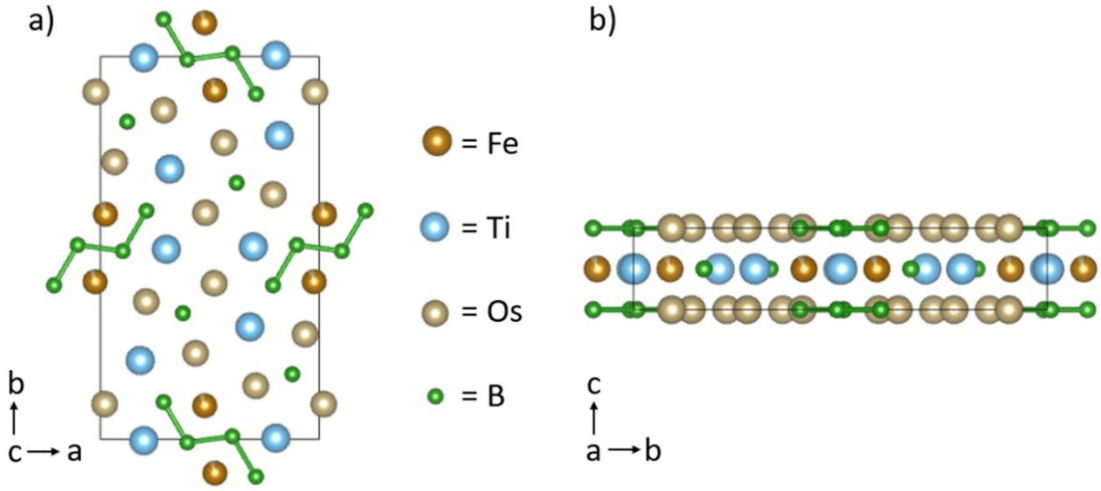

Figure 4.1. Crystal structure of $Ti_2FeOs_3B_3$ viewed along a) [001] and b) [100].

The following parameters were refined: crystal structure factors, lattice constants, peak width, atomic positions, profile and background functions. Occupancies were kept fixed since they did not improve upon the refinement. The position of boron was also kept fixed due to its low scattering factor to X-rays. Figure 2 depicts the Rietveld refinement of the $Ti_2FeOs_3B_3$. The measured pattern is shown in red, the calculated pattern in black, and the intensity difference in blue, with Bragg peak positions indicated in green. Besides the main phase, elemental osmium was also identified. Despite successfully indexing all peaks, there are noticeable intensity mismatches. Since this phase is newly synthesized, the discrepancy is likely due to inaccuracies in vacancies and uncertainties in the substitution of iron with osmium.

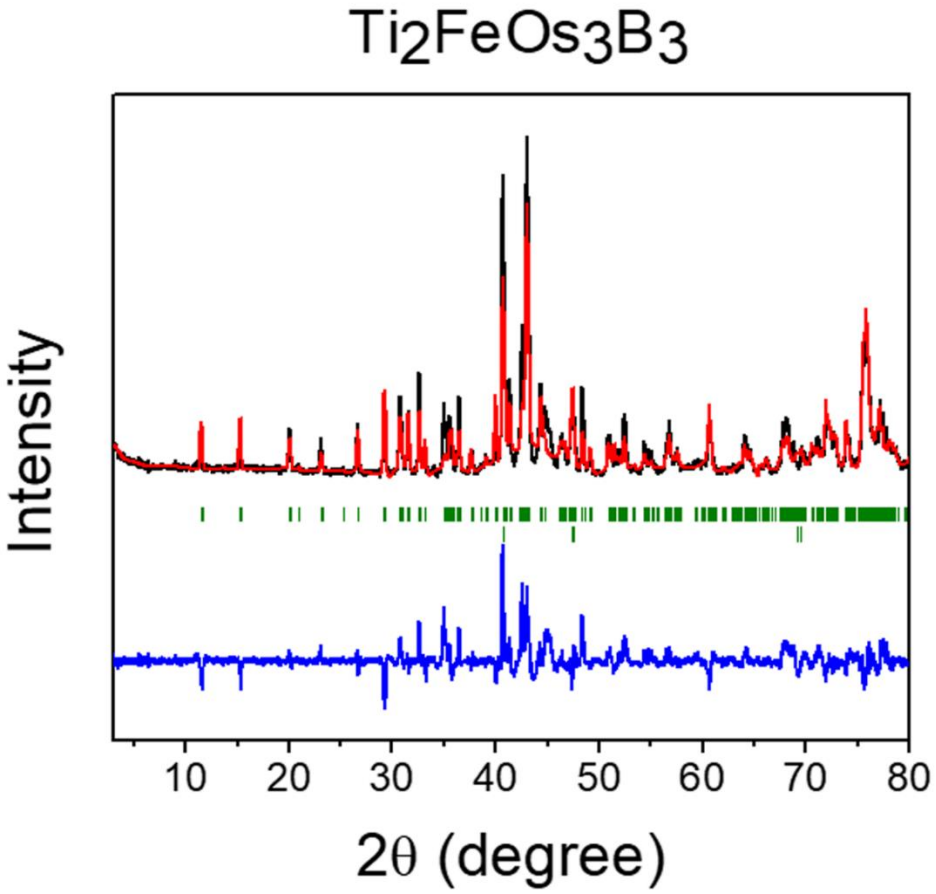

Figure 4.2. Rietveld refinement of the powder XRD sample $Ti_2FeOs_3B_3$. The red curve is the measured pattern, the black curve is the calculated pattern, and the blue curve is the intensity difference. Bragg peak positions are displayed in green.

Table S1 shows the Rietveld Refinement of $Ti_2FeOs_3B_3$. Refined lattice parameters of a = 8.8122(3) Å, b = 15.3844(6) Å, and c = 3.0511(1) Å were obtained with 86% by weight as the main phase. A secondary phase of elemental osmium was identified and estimated to be around 14%. Compared to the iridium-containing compound by Dr. C. Görens[13], $Ti_2Fe_{0.91(1)}Ir_{3.09(1)}B_3$, where a = 8.618(1) Å, b = 14.975(7) Å, and c = 3.221(1) Å, the a and b lattice parameters have increased while c has decreased for $Ti_2FeOs_3B_3$. The volume also reduced from 415.7(2) Å to 413.64(2) Å after osmium incorporation.

Theoretical calculations based on the generalized gradient approximation (GGA), which tends to overestimate values, yielded considerably smaller results for the lattice parameters (**Table 1**). This suggests the likelihood of a mixed occupation at the Fe site with the larger Os or Ti atoms, contributing to the observed discrepancies.

The crystal is built up of two different layers along the [0 0 1] direction. The z = 0 layer contains the B_4 zigzag fragments along with the osmium atoms. The z = ½ layer contains the isolated boron atoms, iron dumbbells, and the titanium atoms. The B_4 unit has a central B2-B2 bond length of 1.8318(3) Å and B1-B2 bond lengths of 1.8815(3) Å. Similarly, in the metal-rich boride $Ti_{1+x}Rh_{2-x+y}Ir_{3-y}B_3$, a B_4 combination is found. It contains a central B2–B2 bond length of 1.81(2) Å and two slightly larger B1–B2 bonds with a bond length of 1.87(3) Å.[8] Both compounds have similar B_4 units with slightly larger B_1-B_2 bonds, implying a consistent pattern in the bonding arrangement of boron atoms. The other main characteristic in this compound is that $Ti_2FeOs_3B_3$ has Fe_2 dumbbells with an intrachain distance of 2.57(4) Å. They are aligned along the [0 0 1] direction, forming ladders in the c direction and separated by 3.05090(11) Å. $Ti_9Fe_2Ru_{18}B_8$, another complex boride, also has this unique feature of one-dimensional Fe_2 dumbbell (Fe ladders) along the c axis. It contains an Fe-Fe distance of 2.489(2) Å, and the Fe_2-Fe_2 distance between two dumbbells is 2.968(1) Å.[12] These iron dumbbells are responsible for the ferromagnetic ordering observed between 10 and 200 K in $Ti_9Fe_2Ru_{18}B_8$. Though the distance between the Fe_2 dumbbells is a bit further, $Ti_2FeOs_3B_3$ is highly likely to exhibit ferromagnetic ordering as well.

Table 4.1. Lattice parameters, B-B, and Fe-Fe bond distances for experimental (exp) $Ti_2FeOs_3B_3$ compared to the theoretical (th) antiferromagnetic (AFM1) model.

	$Ti_2FeOs_3B_3$ (exp)	**$Ti_2FeOs_3B_3$ (th)**
Lattice parameters (Å)	a = 8.8122(3)	a = 8.7058
	b = 15.3845(6)	b = 15.2958
	c = 3.0511(1)	c = 3.0182
B1-B2 bond distance (Å)	1.8815(3)	1.8362
B2-B2 bond distance (Å)	1.8318(3)	1.7774
Fe-Fe bond distance (Å)	2.57(4)	2.7381
Fe_2-Fe_2 bond distance (Å)	3.05090(11)	3.0461

4.6 Theoretical Calculations

Total energies of three different magnetic models were considered to establish the ground state: antiferromagnetic 1 (AFM1), antiferromagnetic 2 (AFM2), ferromagnetic (FM). These models were also compared to the nonmagnetic (NM) state. The experimentally obtained $Ti_2FeOs_3B_3$ was used as the model structure. Figure 3 displays the three magnetic models along the a-axis. In the FM model, all electrons are oriented spin up. AFM1 considers Fe1 and Fe2 to have both electron spins up, while Fe3 and Fe4 are spin down orientation. AFM2 considers Fe1 as spin up while Fe2 is spin down. Similarly, Fe3 is spin up and Fe4 is spin down. Table S2 displays the relative energies of all the calculated models. AFM1 was the most stable structure followed by FM at +8.3054

meV/f.u. AFM2 was the least stable out of all the models. The calculated magnetic moment was 0.530 μB per Fe-atom, whereas it was 1.532 μB per Fe-atom for the AFM2 scenario. This weaker moment on the iron site means there are less unpaired electrons available, which is not preferred in this crystal. Lattice parameters and lengths of B_4 units were thus extracted from the AFM1 model and is depicted in Table 1 along with the experimental values from the Rietveld refinement. All theoretical lattice parameters and bond lengths were smaller than the experimental values. As stated previously, mixed occupation at the Fe site with the larger Os or Ti atoms could be the cause.

As seen in $TiFe_{0.64(1)}Os_{2.36(1)}B_2$, the calculated ground state was also AFM, but is only more stable than the FM structure with a difference of 1.9 meV. Exchange interactions within the metal triangles were FM, but the intrachain interactions favored AFM.[16] In another metal-rich boride involving osmium, $Ti_{5-x}Fe_{1-y}Os_{6+x+y}B_6$, the magnetic ground state was calculated to be AFM, with FM Fe-Fe interactions within and between Fe-chains. There was a close competition overall between the magnetic models as they were within 10 meV from each other.[17] This small energy difference could be affected by external factors such as magnetic field or other environmental conditions, highlighting the intricate nature of these magnetic interactions.

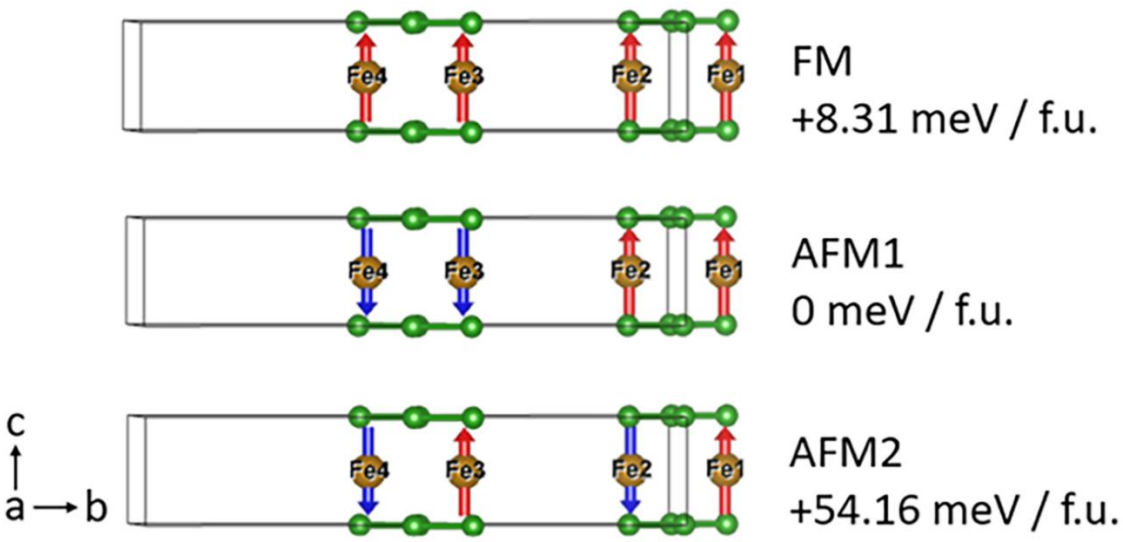

Figure 4.3. Ferromagnetic (FM) and antiferromagnetic (AFM1 and AFM2) models of $Ti_2FeOs_3B_3$ viewed along [100] along with relative energies of the magnetic models.

Figure 4 presents the density of states (DOS) for $Ti_2FeOs_3B_3$ in the nonmagnetic and antiferromagnetic configurations. In the nonmagnetic DOS, a pseudogap, indicated by a local minimum, appears near the Fermi level (E_F). Total states are at 8.43 states/eV in the non-spin-polarized system and drops down to 7.45 states/eV in the antiferromagnetic system, indicating preference for magnetic ordering. Potential mixed occupancies involving Ti in the Fe position or Fe occupying one of the B positions could lead to a significant displacement of the Fermi energy towards larger densities, resulting in the formation of an electronically less stable system in the nonmagnetic case. Similarly, in a different quaternary system of the same elements, $Ti_{5-x}Fe_{1-y}Os_{6+x+y}B_6$,[17] partial DOS curves reveal that Fe is contributing mostly to the peaks at E_F. Spin-polarized calculations show reduced number of states at E_F vs a non-spin polarized scenario, suggesting magnetic ordering is favored for $Ti_{5-x}Fe_{1-y}Os_{6+x+y}B_6$ as well.

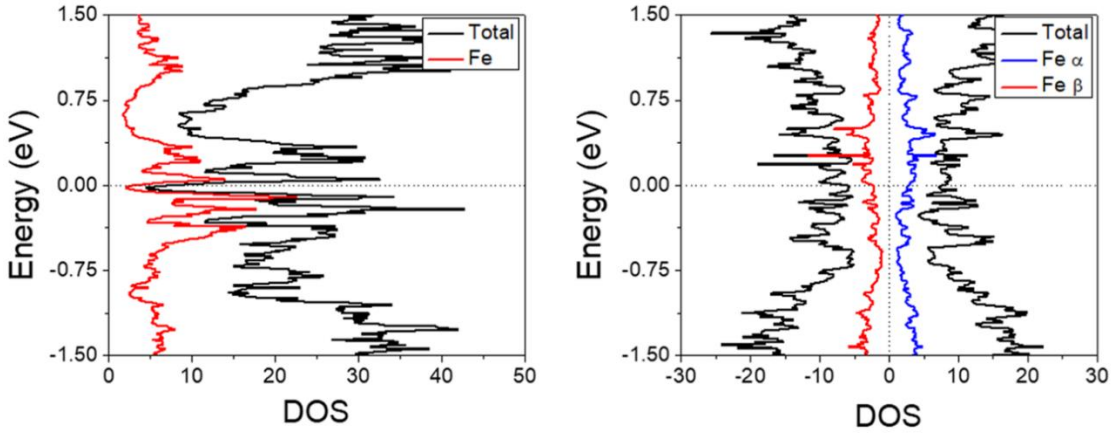

Figure 4.4. (a) Non-spin-polarized and (b) spin-polarized DOS $Ti_2FeOs_3B_3$.

4.7 Magnetic Results and Discussion

The synthesized sample exhibits a strong attraction to an external magnetic field from a magnet at room temperature, indicating the presence of long-range ferromagnetic interactions. Given the small energy disparity (ca. 8 meV) between the predicted magnetic ground state AFM1 and the FM state, a minor alteration in composition can tip the balance towards FM. From the magnetic susceptibility curve depicted in Figure 5a, an AFM transition is revealed at low temperature. However, at high magnetic fields the FM state dominates as seen by the magnetization curve in Figure 5b, leading to a saturation magnetization at 5 K is ~0.32 μB. $Ti_2FeOs_3B_3$ is expected to have a total moment of 1.45 μB from the DFT calculations. The observed magnetization is weak due to the presence of elemental osmium as a side phase in the synthesized product. Moreover, the model for the calculations assumes full occupancy for iron, which does not accurately reflect the real

scenario. These behaviors concur with the DFT calculations performed, with AFM being the ground state, but the relatively weak interchain AFM interactions can be easily overcome by external factors such as the high magnetic field in this case. This phenomenon has also been observed before in the case of ferromagnetic $TiFe_{1-x}Os_{2+x}B_2$[10]. The magnetic ground state was calculated to be AFM, with the FM model only 1.9 meV higher in energy. The bulk powder was ferromagnetic at room temperature, as verified via magnetization measurements. In another scenario, $Hf_2MnRu_5B_2$, the most stable calculated model was FM by 3.86 meV over the AFM model.[18] However, at low field AFM ordering occurred. This transition disappears at high magnetic fields and a FM state emerges, indicating metamagnetic behavior. Since the competition between the AFM and FM ground states is small, external influence can shift the preference in either direction.

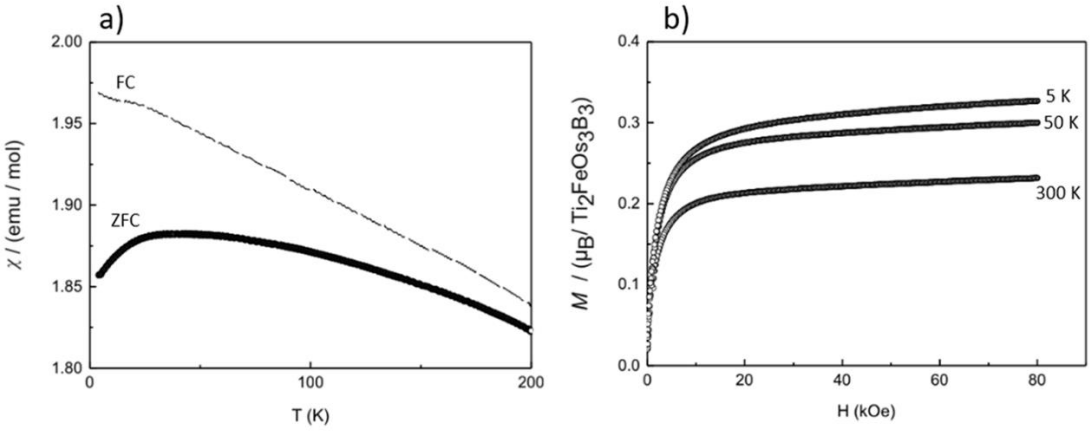

Figure 4.5. (a) Magnetic susceptibility versus temperature and (b) magnetization vs magnetic field measured at 5, 50, and 500 K for $Ti_2FeOs_3B_3$.

4.7 Conclusion

$Ti_2FeOs_3B_3$ has been successfully synthesized and was investigated for its magnetic attributes. Distinguished by its B_4 zigzag fragments, iron dumbbell chains (Fe ladders), and osmium content, theoretical calculations indicate the antiferromagnetic state as energetically favored. Intriguingly, the material demonstrates pronounced reactivity to an external magnetic field at room temperature. An antiferromagnetic transition is apparent at lower temperatures. However, under the influence of strong magnetic fields, the ferromagnetic state prevails. The slight energy differential (approximately 8 meV) between the anticipated AFM1 and FM magnetic ground states implies that even minor adjustments can tip the balance toward a ferromagnetic state. This study contributes to a more comprehensive understanding of the compound's intricate nature.

References

[1] Fokwa BPT. Borides: Solid-State Chemistry. Encycl. Inorg. Bioinorg. Chem., John Wiley & Sons, Ltd; 2014, p. 1–14. https://doi.org/10.1002/9781119951438.eibc0022.pub2.

[2] Villars, P., L. D. Calvert. Pearson's Handbook of Crystallographic Data for Intermetallic Phases ASTM International. Newburry, OH: 1991.

[3] Kuz'ma, Yu B., Ya P. Yarmolyuk. Crystal structure of the compound Ti3Co5B2. J Struct Chem 1971;12:422–4.

[4] Ade M. Synthesis and crystal structures of the new metal-rich ternary borides Ni12AlB8, Ni12GaB8 and Ni10.6Ga0.4B6—examples for the first B5 zig-zag chain fragment. J Solid State Chem 2010.

[5] Scheifers JP, Zhang Y, Fokwa BPT. Boron: Enabling Exciting Metal-Rich Structures and Magnetic Properties. Acc Chem Res 2017;50:2317–25. https://doi.org/10.1021/acs.accounts.7b00268.

[6] KRIPYAKE. PI, Yu B. Kuzma, MV CHEPIGA. CRYSTAL-STRUCTURE OF (RE, CO) 7B4 COMPOUND. DOPOVIDI Akad NAUK Ukr RSR 1972;9:856.

[7] Fokwa, Boniface PT, Martin Hermus. All-Boron Planar B 6 Ring in the Solid-State Phase Ti 7 Rh 4 Ir 2 B 8. Angew Chem Int Ed 2012;7:1702–5.

[8] Goerens C, Fokwa BPT. The complex metal-rich boride Ti1+xRh2−x+yIr3−yB3 (x=0.68, y=1.06) with a new structure type containing B4 zigzag fragments: Synthesis, crystal chemistry and theoretical calculations. J Solid State Chem 2012;192:113–9. https://doi.org/10.1016/j.jssc.2012.04.005.

[9] Mbarki M, St. Touzani R, Fokwa BPT. Unexpected Synergy between Magnetic Iron Chains and Stacked B6 Rings in Nb6Fe1−xIr6+xB8. Angew Chem Int Ed 2014;53:13174–7. https://doi.org/10.1002/anie.201406397.

[10] Jan Philip Scheifers. Designing New Structures of Magnetic Materials: Cases of Metal Borides and Metal Chalcogenides. Diss 2020.

[11] Spin Frustration and Magnetic Ordering from One-Dimensional Stacking of Cr3 Triangles in TiCrIr2B2 n.d. https://doi.org/10.1021/acs.inorgchem.6b00714.

[12] Fokwa BPT, Samolyuk GD, Miller GJ, Dronskowski R. Ladders of a Magnetically Active Element in the Structure of the Novel Complex Boride $Ti_9Fe_2Ru_{18}B_8$: Synthesis, Structure, Bonding, and Magnetism. Inorg Chem 2008;47:2113–20. https://doi.org/10.1021/ic7020963.

[13] Goerens, Christian. Synthese und Charakterisierung von komplexen Iridium-Boriden mit B4-Einheiten. Diss 2013;Aachen, Techn. Hochsch.

[14] Perdew JP, Burke K, Ernzerhof M. Generalized Gradient Approximation Made Simple. Phys Rev Lett 1996;77:3865–8. https://doi.org/10.1103/PhysRevLett.77.3865.

[15] Kresse G, Furthmüller J. Efficient iterative schemes for *ab initio* total-energy calculations using a plane-wave basis set. Phys Rev B 1996;54:11169–86. https://doi.org/10.1103/PhysRevB.54.11169.

[16] Scheifers JP, Flores JH, Janka O, Pöttgen R, Fokwa BPT. Triangular Arrangement of Ferromagnetic Iron Chains in the High-TC Ferromagnet TiFe1−xOs2+xB2. Chem – Eur J 2022;28:e202201058. https://doi.org/10.1002/chem.202201058.

[17] Scheifers JP, Küpers M, Bakshi NG, Touzani RSt, Gladisch FC, Rodewald UCh, et al. Fe- and B-Chains in the Ti $_{5-x}$ Fe $_{1-y}$ Os $_{6+x+y}$ B $_{6}$ Structure Type Derived from Chemical Twinning of the Nb $_{1-x}$ Os $_{1+x}$ B Type: Experimental and Computational Investigations. Inorg Chem 2023;62:8670–7. https://doi.org/10.1021/acs.inorgchem.3c00837.

[18] Shankhari P, Zhang Y, Stekovic D, Itkis ME, Fokwa BPT. Unexpected Competition between Antiferromagnetic and Ferromagnetic States in Hf2MnRu5B2: Predicted and Realized. Inorg Chem 2017;56:12674–7. https://doi.org/10.1021/acs.inorgchem.7b01758.

Chapter 5:

Computational Investigation on $Hf_2MOs_5B_2$ (M = Fe, Mn)

In this chapter, we use DFT to investigate the possibility of two new potential phases in the $Ti_3Co_5B_2$ structure type: quaternaries $Hf_2FeOs_5B_2$ and $Hf_2MnOs_5B_2$.

5.1 Introduction

Solid-state chemists continuously face the ongoing challenge of seeking out new materials that exhibit exceptional physical properties. Several quaternary intermetallic borides of the $Ti_3Co_5B_2$-type structure with the general formula $A_2MM'_5B_2$ (A = Mg, Sc; M = main-group metal or 3d element such as Fe, Co; M' = Ru, Rh, Ir) have been investigated with respect to itinerant magnetism.[1,2] Those with magnetically active 3d elements have attracted interest because they form well separated, one-dimensional chains that exhibit ferromagnetic (e.g., $Sc_2FeRh_5B_2$) or antiferromagnetic (e.g., $Mg_2MnRh_5B_2$) behavior. The potential for adjusting this compound offers a chance to explore possible applications in data storage and retrieval.

The foundation of new material discoveries lies in newly developed compounds. The origins of breakthroughs in high critical temperature superconductors or thermoelectric materials can be traced back to the identification of compounds that were previously undiscovered.[3,4] Grasping the capability of these undiscovered compounds in nature is a topic of both scientific and technological importance. Density functional theory (DFT) and its extensions have proven to be effective in accurately modeling the

ground-state and finite temperature behavior of various compounds. These calculations have also demonstrated efficient and accurate prediction of phase stability in numerous chemistries.[5–8] Approximate models for the energy functional have yielded accurate predictions for many classes of materials. This allows the physical laws of quantum physics to be connected to the technologically relevant properties of materials. The exponential growth in computing power has enabled a paradigm shift in computational materials science with DFT. Theoretical scientists can now not only explain and interpret material properties but also play a crucial role in predicting novel materials with specific functionalities for various applications.[8]

DFT reformulates the wavefunction equation, which describes the behavior of electrons in a system, such that the approximate solutions are tractable for realistic materials. Inputs of a DFT calculation include coordinates and identities of the atoms in the material within a repeating lattice, the exchange-correlation functional, parameters and algorithms for numerical and iterative convergence, and optional methods for more efficiently treating the core electrons in the system. Outputs include electronic charge density, total energy, magnetic configuration, and electronic band structure. The use of DFT techniques to interpret and predict the properties of materials has grown tremendously because of the availability of easy-to-use computer codes (both commercial and open source), faster and more stable mathematical algorithms for solving DFT equations, and low-cost and widely available computing resources. There are databases that contain the results of thousands of calculations that are publicly available such as

Materials Project, Open Quantum Materials Database, and the Computational Materials Repository.[8–13]

To identify and investigate potential new materials, it is necessary to determine which chemical compositions are likely to form compounds. The principle underlying computational crystal structure prediction is energy minimization: that is, to identify the atomic arrangement that yields a global minimum in energy under the desired thermodynamic constraints.[14] One popular approach involves evaluating the energy of the candidates' crystal structures and selecting the lowest-energy candidate as the 'best guess' solution. In order to improve efficiency, partial experimental information can also be used to enforce constraints on symmetry.[8]

Our group recently discovered the new quaternaries $Hf_2FeIr_5B_2$ and $Hf_2MnIr_5B_2$ as displayed in Figure 1.

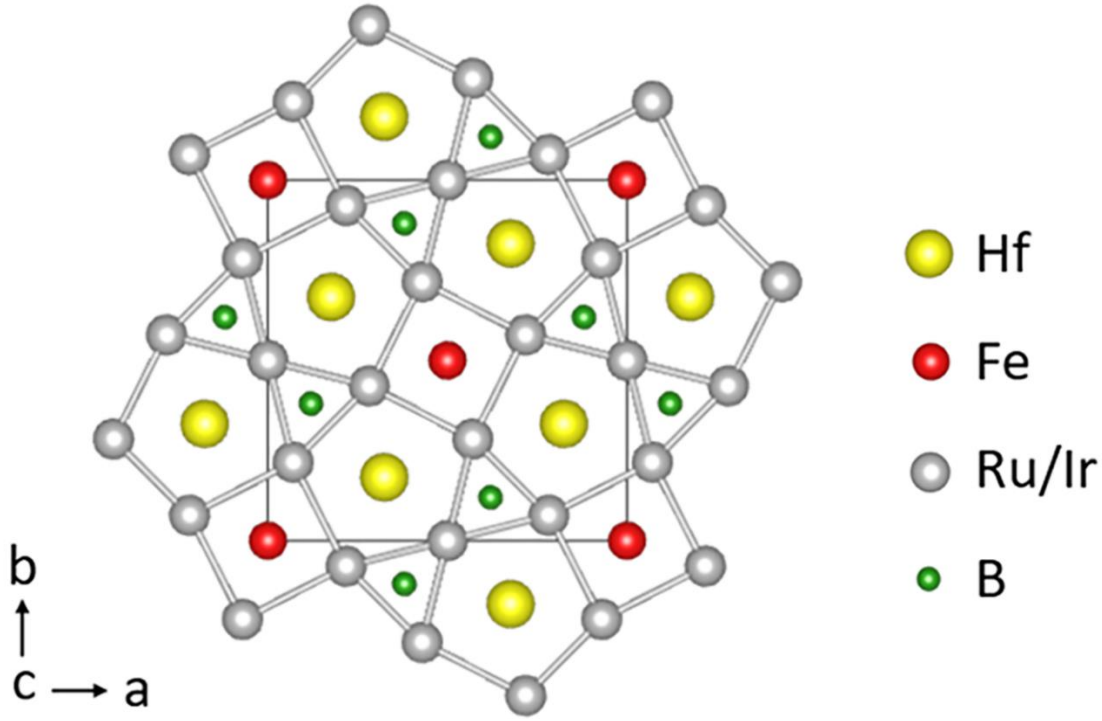

Figure 5.1. Crystal structure of quaternaries $Hf_2MIr_5B_2$ (M = Fe, Mn) viewed along [001].

$Hf_2FeIr_5B_2$ has a high ordering temperature of T_C = 900 K, coercivity Hc = 12.1 kA/m, and exhibited hysteresis above room temperature, a prerequisite as a permanent magnetic material for future applications. This compound has strong FM interchain spin-exchange interaction, preventing nearby chains from flipping their individual spins and thus giving a large Curie temperature. $Hf_2MnIr_5B_2$ is metamagnetic and has two ordering temperatures of T_C = 590 K and T_N = 30 K. The Mn-Mn interchain coupling is more antiferromagnetic by 60.01 meV/f.u. versus the ferromagnetic state, giving rise to a large coercivity value of Hc = 62.0 kA/m.[15] Possible new potential compounds would be replacing iridium with osmium since both have similar atomic radius and are 5d metals. With only one less valence electron than iridium, introducing osmium could present new

insight in this structure type. Ruthenium substitution has been performed previously with iridium, but dominating antiferromagnetic interactions were observed. Osmium, being a 5d metal, could introduce large spin-orbit-coupling that may enhance the magnetic properties. In the case of $TiFe_{0.64(1)}Os_{2.36(1)}B_2$, this compound consists of trigonal-planar B_4 boron fragments interacting with M_3-triangles (M = 64% Fe + 36% Os), forming strong ferromagnetic interactions.[16] The work reported herein focuses on ab initio calculations to search for possible new magnetic materials within the $Ti_3Co_5B_2$ structure type, namely quaternaries $Hf_2FeOs_5B_2$ and $Hf_2MnOs_5B_2$.

5.2 Results & Discussion

Starting with structures $Hf_2FeIr_5B_2$ and $Hf_2MnIr_5B_2$, osmium was used to replace iridium in both these compounds. Crystallizing in the tetragonal space group P4/mbm, these structures can be described as face-connected tetragonal, pentagonal, and edge-sharing double trigonal prisms. These prisms stack along the c-direction, building channels. Osmium occupies the 8j and 2c site in both cases, forming the prisms that other atoms will inhabit. The pentagonal 4g site is occupied by the bigger hafnium atoms, and the trigonal 4g site is occupied by the small boron atoms. The difference in the structures is whether iron or manganese will occupy the tetragonal 2a site.

Calculations were performed on a nonmagnetic (NM), ferromagnetic (FM), and antiferromagnetic (AFM) system to determine which is the lowest in energy. Table 1 displays the relative energy difference between all three systems. In both cases, the non-

spin polarized systems were higher in energy versus the magnetic counterparts. Thus, these compounds prefer magnetic ordering. $Hf_2FeOs_5B_2$ is predicted to be AFM in the ground state by 40 meV over the FM counterpart. The calculated magnetic moment is 2.41 μB per Fe-atom. In the case of $Hf_2MnOs_5B_2$, this is more stable in the FM ground state by 20 meV over the AFM counterpart. The calculated magnetic moment obtained is 2.51 μB per Mn-atom. For $TiFe_{0.64(1)}Os_{2.36(1)}B_2$, the calculated magnetic moment obtained was 1.84 μB per Fe-atom.[16] The relatively higher magnetic moment for $Hf_2MnOs_5B_2$ implies that this will likely exhibit stronger ferromagnetic behavior.

Table 5.1. Relative energy calculations between nonmagnetic (NM), antiferromagnetic (AFM), and ferromagnetic (FM) models.

Compound	**E_{NM} (meV)**	**E_{AFM} (meV)**	**E_{FM} (meV)**
$Hf_2FeOs_5B_2$	+1,460	0	+40
$Hf_2MnOs_5B_2$	+1,180	+20	0

GGA+SOC calculations were applied as described by Zhang et al. for calculations within the $Ti_3Co_5B_2$-type structure. [17] Magnetic anisotropy is when spins tend to prefer a particular orientation over others and arises through spin-orbit coupling (SOC). Total magnetocrystalline anisotropy energy (E_{MAE}) comes from two contributions: magnetic anisotropy energy (E_{SOC}) from SOC and long-range magnetic dipole-dipole interaction energy (E_{MDD}):

$$E_{MAE} = E_{SOC} + E_{MDD}$$

E_{MDD} makes relatively very small contributions to E_{MAE} compared with SOC, and thus the net E_{SOC} is approximately equal to E_{MAE}.[18,19] A tetragonal system has either an easy magnetization axis (c-axis) or an easy magnetization plane (ab-plane) depending on the sign of the anisotropy constants.[20] Thus, the total energy difference between magnetization parallel to the c-axis (∥c) and perpendicular to the c-axis (⊥c) is defined as MAE, i.e.,

$$E_{MAE} \approx E_{SOC} = E(\|c) - E(\perp c)$$

Spin exchange energy (E_{ex}) is estimated from the energy difference between ferromagnetic and the antiferromagnetic spin orientations.

Table 2 displays the E_{SOC} and E_{ex} of the previous reported compounds and the calculations for the new predicted structures. Based on the E_{ex}, $Hf_2FeOs_5B_2$ prefers AFM ordering while $Hf_2MnOs_5B_2$ prefers FM ordering, which agrees with the ground state energy calculations. Compared to $Hf_2FeIr_5B_2$, $Hf_2FeOs_5B_2$ has a lower E_{ex} and E_{SOC}. Even though $Hf_2FeOs_5B_2$ has lower values, it would still be a good magnet candidate since magnetic anisotropy is relatively large at -2.13 meV/f.u. It has been studied that Ru-rich quaternary phases (with less than 63 VE) display dominating AFM interactions whereas Ir-rich phases (with more than 63 VE) are dominated by FM interactions if the magnetic element is Fe.[21–23] $Hf_2FeIr_5B_2$, with a valence electron of 67, falls into the FM category, whereas $Hf_2FeOs_5B_2$, with a valence electron of 62, falls into the AFM category. The current calculations agree with previous reported data in terms of valence electron (VE) count. In contrast to the Fe-based compounds, the Mn-based compounds do not show a VE-dependent trend and are unpredictable. $Hf_2MnOs_5B_2$ (61 VE) favors FM

ordering and has spins along the easy plane. Meanwhile, $Hf_2MnIr_5B_2$ (66 VE) prefers AFM interactions and has an easy c axis. Even though $Hf_2MnOs_5B_2$ has a lower exchange energy, it has a higher spin-orbit coupling and thus higher magnetic anisotropy.

Table 5.2. Theoretical calculations of E_{SOC} and E_{ex} of $Hf_2MIr_5B_2$ (M = Fe, Mn) and $Hf_2MOs_5B_2$ (M = Fe, Mn).

Compound	E_{ex} (meV/f.u.)	E_{SOC} (meV/f.u.)
$Hf_2FeIr_5B_2$	+40.19	+3.27
$Hf_2MnIr_5B_2$	−60.01	−1.55
$Hf_2FeOs_5B_2$	-20.36	-2.13
$Hf_2MnOs_5B_2$	+5.92	+1.92

5.3 Conclusion

In summary, the work reported focuses on VASP calculations of quaternaries $Hf_2FeOs_5B_2$ and $Hf_2MnOs_5B_2$. Both compounds have preference for magnetic ordering, with $Hf_2FeOs_5B_2$ preference for AFM and $Hf_2MnOs_5B_2$ with preference for FM. $Hf_2FeOs_5B_2$ has an E_{ex} of -20.36 meV/f.u. and SOC of -2.13 meV/f.u., whereas $Hf_2MnOs_5B_2$ has an E_{ex} of +5.92 meV/f.u. and SOC of +1.92 meV/f.u. Out of these two compounds, $Hf_2FeOs_5B_2$ has the most promising potential since exchange energy and spin-orbit coupling are both greater.

References:

[1] Nagelschmitz EA, Jung W. Scandium Iridium Boride $Sc_3Ir_5B_2$ and the Quaternary Derivatives $Sc_2MIr_5B_2$ with M = Be, Al, Si, Ti, V, Cr, Mn, Fe, Co, Ni, Cu, Ga, or Ge: Preparation, Crystal Structure, and Physical Properties. Chem Mater 1998;10:3189–95. https://doi.org/10.1021/cm9802898.

[2] Eibenstein U, Jung W. Zn11Rh18B8 and Zn10MRh18B8 with M = Sc, Ti, V, Cr, Mn, Fe, Co, Ni, Cu, Al, Si, Ge, Sn – New Ternary and Quaternary Zinc Rhodium Borides. Z Für Anorg Allg Chem 1998;624:802–6. https://doi.org/10.1002/(SICI)1521-3749(199805)624:5<802::AID-ZAAC802>3.0.CO;2-A.

[3] G. Jeffrey Snyder, Eric S. Toberer. Complex thermoelectric materials. Nature Mater 2008:105–8.

[4] Bartsch T, Hoffmann R-D, Pöttgen R. The quaternary arsenide oxides $Ce_9Au_{5-x}As_8O_6$ and $Pr_9Au_{5-x}As_8O_6$. Z Für Naturforschung B 2016;71:1245–52. https://doi.org/10.1515/znb-2016-0160.

[5] Hart GLW, Forcade RW. Generating derivative structures from multilattices: Algorithm and application to hcp alloys. Phys Rev B 2009;80:014120. https://doi.org/10.1103/PhysRevB.80.014120.

[6] Ozoliņš V, Wolverton C, Zunger A. Cu-Au, Ag-Au, Cu-Ag, and Ni-Au intermetallics: First-principles study of temperature-composition phase diagrams and structures. Phys Rev B 1998;57:6427–43. https://doi.org/10.1103/PhysRevB.57.6427.

[7] Ong SP, Wang L, Kang B, Ceder G. $Li–Fe–P–O_2$ Phase Diagram from First Principles Calculations. Chem Mater 2008;20:1798–807. https://doi.org/10.1021/cm702327g.

[8] Jain A, Shin Y, Persson KA. Computational predictions of energy materials using density functional theory. Nat Rev Mater 2016;1:15004. https://doi.org/10.1038/natrevmats.2015.4.

[9] Curtarolo S, Setyawan W, Wang S, Xue J, Yang K, Taylor RH, et al. AFLOWLIB.ORG: A distributed materials properties repository from high-throughput ab initio calculations. Comput Mater Sci 2012;58:227–35. https://doi.org/10.1016/j.commatsci.2012.02.002.

[10] Kirklin S, Saal JE, Meredig B, Thompson A, Doak JW, Aykol M, et al. The Open Quantum Materials Database (OQMD): assessing the accuracy of DFT formation energies. Npj Comput Mater 2015;1:15010. https://doi.org/10.1038/npjcompumats.2015.10.

[11] Jain A, Ong SP, Hautier G, Chen W, Richards WD, Dacek S, et al. Commentary: The Materials Project: A materials genome approach to accelerating materials innovation. APL Mater 2013;1:011002. https://doi.org/10.1063/1.4812323.

[12] Jain A, Hautier G, Moore CJ, Ping Ong S, Fischer CC, Mueller T, et al. A high-throughput infrastructure for density functional theory calculations. Comput Mater Sci 2011;50:2295–310. https://doi.org/10.1016/j.commatsci.2011.02.023.

[13] Landis DD, Hummelshøj JS, Nestorov S, Greeley J, Dułak M, Bligaard T, et al. The Computational Materials Repository. Comput Sci Eng 2012;14:51–7. https://doi.org/10.1109/MCSE.2012.16.

[14] Oganov AR, Valle M. How to quantify energy landscapes of solids. J Chem Phys 2009;130:104504. https://doi.org/10.1063/1.3079326.

[15] Shankhari P, Janka O, Pöttgen R, Fokwa BPT. Rare-Earth-Free Magnets: Enhancing Magnetic Anisotropy and Spin Exchange Toward High-TC Hf2MIr5B2 (M = Mn, Fe). J Am Chem Soc 2021;143:4205–12. https://doi.org/10.1021/jacs.0c10778.

[16] Scheifers JP, Flores JH, Janka O, Pöttgen R, Fokwa BPT. Triangular Arrangement of Ferromagnetic Iron Chains in the High-TC Ferromagnet TiFe1−xOs2+xB2. Chem – Eur J 2022;28:e202201058. https://doi.org/10.1002/chem.202201058.

[17] Zhang Y, Miller GJ, Fokwa BPT. Computational Design of Rare-Earth-Free Magnets with the Ti3Co5B2-Type Structure. Chem Mater 2017;29:2535–41. https://doi.org/10.1021/acs.chemmater.6b04114.

[18] Błoński P, Hafner J. Magnetic anisotropy of transition-metal dimers: Density functional calculations. Phys Rev B 2009;79:224418. https://doi.org/10.1103/PhysRevB.79.224418.

[19] Koo H-J, Xiang H, Lee C, Whangbo M-H. Effect of Magnetic Dipole−Dipole Interactions on the Spin Orientation and Magnetic Ordering of the Spin-Ladder Compound $Sr_3Fe_2O_5$. Inorg Chem 2009;48:9051–3. https://doi.org/10.1021/ic9007526.

[20] Getzlaff M. Fundamentals of Magnetism. Springer Science & Business Media; 2007.

[21] Samolyuk GD, Fokwa BPT, Dronskowski R, Miller GJ. Electronic structure, chemical bonding, and magnetic properties in the intermetallic series $Sc_2Fe(Ru_{1-x}Rh_x)_5B_2$ from first principles. Phys Rev B 2007;76:094404. https://doi.org/10.1103/PhysRevB.76.094404.

[22] Fokwa BPT, Lueken H, Dronskowski R. Rational Synthetic Tuning between Itinerant Antiferromagnetism and Ferromagnetism in the Complex Boride Series Sc2FeRu5−nRhnB2 (0≤n≤5). Chem – Eur J 2007;13:6040–6. https://doi.org/10.1002/chem.200700128.

[23] Hermus M, Yang M, Grüner D, DiSalvo FJ, Fokwa BPT. Drastic Change of Magnetic Interactions and Hysteresis through Site-Preferential Ru/Ir Substitution in $Sc_2FeRu_{5-x}Ir_xB_2$. Chem Mater 2014;26:1967–74. https://doi.org/10.1021/cm500237h.

Chapter 6:

Conclusion

This dissertation has undertaken the ambitious task of developing innovative magnetic materials rooted in the $Ti_3Co_5B_2$ structure type while avoiding the use of rare-earth elements. The exploration has led to significant findings that hold promise for various applications.

Beginning with the synthesis of $Hf_2FeIr_5B_2$, a quaternary boride that showcased magnetic behavior above room temperature, this material holds the potential to be employed as a permanent magnet in future applications. Building upon this foundation, Chapter 3 delved into the study of the $Hf_2Fe_{1-\delta}Ir_{5-x+\delta}Ru_xB_2$ series, revealing the relationship between magnetic characteristics, valence electron count, and the role of hafnium. The varied magnetization behaviors observed, from soft to semi-hard magnetic characteristics, hint at their potential versatility in different applications. Chapter 4 focuses on the synthesis, characterization, and magnetic properties of $Ti_2FeOs_3B_2$, showcasing its unique features such as B_4 zigzag fragments and iron dumbbell chains. Theoretical calculations highlighted its antiferromagnetic behavior, yet its responsiveness to external magnetic fields added layers of complexity to its magnetic nature. Lastly, Chapter 5 delved into the exploration of $Hf_2MOs_5B_2$ (M = Mn, Fe), unveiling the magnetic potential of these new compounds. $Hf_2FeOs_5B_2$ displayed a preference for antiferromagnetic ordering, while $Hf_2MnOs_5B_2$ exhibited a preference for ferromagnetic ordering.

In conclusion, this dissertation has significantly advanced our understanding of novel magnetic materials. The interplay of magnetic behaviors, structural complexities, and theoretical insights presented here offers a foundation for further exploration, optimization, and practical utilization of these materials.